

Kinematics of the Envelope and Two Bipolar Jets in the Class 0 Protostellar System L1157

Woojin Kwon^{1,2,3}, Manuel Fernández-López^{2,4}, Ian W. Stephens^{2,5}, and Leslie W. Looney²

wkwon@kasi.re.kr

ABSTRACT

A massive envelope and a strong bipolar outflow are the two main structures characterizing the youngest protostellar systems. In order to understand the physical properties of a bipolar outflow and the relationship with those of the envelope, we obtained a mosaic map covering the whole bipolar outflow of the youngest protostellar system L1157 with about $5''$ angular resolution in CO J=2–1 using the Combined Array for Research in Millimeter-wave Astronomy. By utilizing these observations of the whole bipolar outflow, we estimate its physical properties and show that they are consistent with multiple jets. We also constrain a preferred precession direction. In addition, we observed the central envelope structure with $2''$ resolution in the $\lambda = 1.3$ and 3 mm continua and various molecular lines: C^{17}O , C^{18}O , ^{13}CO , CS, CN, N_2H^+ , CH_3OH , H_2O , SO, and SO_2 . All the CO isotopes and CS, CN, and N_2H^+ have been detected and imaged. We marginally detected the features that can be interpreted as a rotating inner envelope in C^{17}O and C^{18}O and as an infalling outer envelope in N_2H^+ . We also estimated the envelope and central protostellar masses and found that the dust opacity spectral index changes with radius.

Subject headings: circumstellar matter — stars: formation — stars: individual (L1157) — stars: pre-main sequence — techniques: interferometric

¹SRON Netherlands Institute for Space Research, Landleven 12, 9747 AD Groningen, The Netherlands

²Astronomy Department, University of Illinois, 1002 West Green Street, Urbana, IL 61801

³Korea Astronomy and Space Science Institute, 776 Daedeok-daero, Yuseong-gu, Daejeon 34055, Republic of Korea

⁴Instituto Argentino de Radioastronomía, CCT-La Plata (CONICET), C.C.5, 1894, Villa Elisa, Argentina

⁵Institute for Astrophysical Research, Boston University, Boston, MA 02215, USA

1. Introduction

Bipolar outflows are the most energetic and remarkable phenomenon of star formation. Particularly, the youngest protostellar systems, the so-called Class 0 young stellar objects (YSOs), are characterized by a well-developed bipolar outflow with a massive envelope (Andre et al. 1993). At the earliest stage of star formation, material strongly accretes onto the central protostar from the envelope, presumably through an accreting disk. Meanwhile, a bipolar outflow is launched and helps in removing angular momentum of the accreting material. Therefore, investigating the two main structures (envelopes and bipolar outflows) together is crucial for understanding the early stages of star formation and evolution. Note that what we call a bipolar outflow in this paper is a jet ejecting material rather than a slow molecular outflow mainly consisting of the interacting features between the ejected jet and the ambient gas like a bow shock (e.g., Frank et al. 2014). Because of this, the terms outflow and jet are used interchangeably in this paper.

Although much is known about bipolar outflows, such as their general physical and chemical properties, impacts on the environments, and evolutionary changes (e.g., Arce et al. 2007), there remains many unanswered, fundamental questions: What is the launching mechanism? Is it rotating? Is it precessing and if so, what causes the precession? Theoretical studies agree that bipolar outflows are launched magnetocentrifugally (Blandford & Payne 1982; Ferreira et al. 2006; Ferreira 1997; Cerqueira et al. 2006), but the launching mechanism and the launching regions are not yet clear (c.f., X-wind and disk-wind models, Shu et al. 1994; Konigl & Pudritz 2000). Bipolar outflows are expected to be rotating due to magnetocentrifugal launching and angular momentum conservation for the accreting material. Indeed, a small number of previous observational studies toward Class 0 YSOs have reported a velocity gradient across bipolar outflow widths, which can be interpreted as rotation (Pety et al. 2006; Launhardt et al. 2009; Zapata et al. 2010; Choi et al. 2011). However, different interpretations are possible such as multiple jet events (Soker & McIcley 2013). In addition, bipolar outflows often show a wiggling feature, which can be interpreted as precession. However, with the exception of close binary systems, the precession mechanism has not fully been understood (e.g., Teixeira et al. 2008).

L1157-mm is one of the archetypical outflow sources. It is embedded in an isolated star forming cloud located in Cepheus at a distance of 250 pc (Looney et al. 2007, and references therein). With a bipolar outflow oriented nearly on the plane of the sky, L1157 is one of the most extensively investigated Class 0 YSOs over a wide range of wavelengths on various topics. Looney et al. (2007) detected a flattened envelope structure in silhouette using the IRAC data of the *Spitzer Space Telescope* (hereafter *Spitzer*). Kwon et al. (2009) found that grains have significantly grown already at this earliest stage, and the density

distribution has a power-law index of ~ 1.8 toward the L1157 envelope. Further studies at higher angular resolution reported consistent results (Chiang et al. 2012). Recently, dust polarization has also been imaged by the Combined Array for Research in Millimeter-wave Astronomy (CARMA) (Stephens et al. 2013), which nicely shows a clear hourglass morphology centered along the bipolar outflow.

The well-collimated bipolar outflow of L1157 was found over two decades ago (Umemoto et al. 1992). Particularly the southern blue-shifted lobe has been recognized to be heated by shocks, and extensive molecular line studies have followed. For example, time dependent shock chemistry was studied with a single-dish millimeter telescope (e.g., Bachiller & Pérez Gutiérrez 1997; Bachiller et al. 2001). Interferometric millimeter observations at $\sim 3''$ resolution of CO and SiO in the southern lobe have suggested multiple bow shocks (e.g., Gueth et al. 1996; Gueth et al. 1998). In addition Nisini et al. (2010) found that in the shocked region, 20% of all cooling is due to water molecules, and Santangelo et al. (2013) distinguished warm and hot components in the shocked regions using the far-infrared spectroscopic imaging data of the *Herschel Space Observatory*.

In this paper, we study the bipolar outflow and the envelope structure of L1157 using CARMA. We report various molecular line observations as well as continuum at $\lambda = 1.3$ and 3 mm. In particular, we obtained a mosaic map of CO J=2–1 covering the whole area of the L1157 bipolar outflow spanning over $5'$ with $5''$ angular resolution. In addition, based on a multi-jet model fitting to the data cube, we find the physical parameters of the bipolar outflow. We first describe the details of the observations in Section 2. Then, the results of the central envelope area are presented and discussed in Section 3. In Section 4 and 5, we show the outflow mapping image, analyze the data, and discuss the physical meanings. Finally, we enumerate the main conclusions in Section 6.

2. Observations and data reduction

We have obtained continuum and molecular line data toward L1157 using CARMA. The data were taken between 2010 July and October. An additional data set, originally taken as a CARMA summer school project to carry out polarimetric observations toward L1157 in 2011 July (Stephens et al. 2013), has also been included. The observations are summarized in Table 1. For each molecular line transition, Table 2 shows the rest frequencies, synthesized beam size, velocity resolution, and the root-mean square (RMS) noise per channel.

We have observed the entire bipolar outflow spanning over $5'$ in CO J=2–1 using 25 mosaic pointings. When designing the mosaic pattern, we used the *Spitzer* $8\ \mu\text{m}$ image

(Looney et al. 2007). All 25 mosaic points were observed between each of the phase calibrator observations to achieve a constant sensitivity over the entire field. We have employed the most compact CARMA E-array configuration in order to maximize sensitivity for the largest scales possible, i.e., to minimize the missing flux associated with the absence of zero spacing visibilities for interferometric observations. The configuration provides an angular resolution of about $5''$ at $\lambda = 1.3$ mm and is sensitive up to about $20''$ scales given the uv coverage of CARMA (Kwon et al. 2009). Four bands among 8 spectral bands available in CARMA were set to a wide bandwidth of 500 MHz for continuum, and the other four bands were used to observe the spectral lines CO, C¹⁷O, CN, CH₃OH, and H₂O. We have configured the CARMA correlator with a bandwidth of 125 MHz (~ 370 km s⁻¹) and a velocity resolution of about 0.5 km s⁻¹ at $\lambda = 1.3$ mm for all the line observations. The relatively broad bandwidth guaranteed to cover all components of the bipolar outflow with good velocity resolution.

We have also observed the central protostar of L1157 (L1157-mm) in the D-array configuration with a longer integration time at about $2''$ resolution. We employed the same correlator set-up as the bipolar outflow observations.

In addition, we have observed at $\lambda = 3$ mm toward L1157-mm in the C-array configuration to match the angular resolution of the D-array data at $\lambda = 1.3$ mm. We used an 8 MHz band for C¹⁸O and N₂H⁺ (in the lower and upper sideband respectively) and four 31 MHz bands for the other molecular line transitions such as ¹³CO, CH₃OH, SO, and SO₂. The last three bands were set to the wide band of 500 MHz for observing continuum.

We also included the E-array data of the CARMA summer school project, which had the primary goal of studying magnetic fields associated with L1157. The data consist of continuum, CO, and CS at $\lambda = 1.3$ mm. The continuum data were used in the magnetic field studies by Stephens et al. (2013) and the CO data were combined with our large CO data. We also report the results of the CS observations here.

Data have been calibrated following the general procedures using the Multichannel Image Reconstruction, Image Analysis, and Display software (MIRIAD, Sault et al. 1995). The flux of the gain calibrator 1927+739 was determined using a reliable primary flux calibrator (Uranus or MWC349). We obtained 1.7 Jy and 4.8 Jy for the 1927+739 fluxes at $\lambda = 1.3$ and 3 mm, respectively, and used these values for all the data taken in 2010 since the data were taken over a small period of time. On the other hand, we used 1.2 Jy of the 1927+739 flux for the additional data set taken in 2011 which was bootstrapped from its flux calibrator. The absolute flux calibration uncertainties are about 15% and 10% at $\lambda = 1.3$ and 3 mm, respectively (e.g., Kwon et al. 2009). When utilizing the target fluxes for estimating physical parameters in the paper, we take into account only statistical uncertainties. The

natural weighting scheme was employed for image construction. Note that the molecular line data set from 2010 October 17 has been excluded for the final combined images since the observations were taken in poor weather conditions.

The final products of all the observational data are summarized in Table 2. As presented, the angular resolution toward the central envelope is about $2''$ and for the bipolar outflow and the summer school data (CS) about $5''$. The velocity resolutions and sensitivities of individual continuum and molecular lines are also listed in the table. We have not detected any structures in CH_3OH , H_2O , SO , and SO_2 for the achieved sensitivities.

3. Central envelope region

To date, it is still nearly impossible to achieve high angular resolution data with a good sensitivity for directly observing outflow launching regions. A reasonable approach, therefore, is to model the overall features of the bipolar outflow and obtain an insight for the small scale features such as launching regions. In addition, the properties of the launching region may be related to the physical properties of the envelope, which is the reservoir of the accreting material. For example, the kinematics of the envelope are expected to match those of the bipolar outflow launching regions. In this section we show and discuss the results of the envelope properties, and the observational and modeling results of the bipolar outflow are presented in the next section with an interpretation connecting the two structures.

3.1. Continuum emission

The $\lambda = 1.3$ and 3 mm continuum maps are presented in Figure 1. In addition, the rightmost panel shows the dust opacity spectral index (β) map with the assumption of optically thin emission: dust mass absorption coefficient $\kappa_\nu \propto \nu^\beta$. As the Rayleigh-Jeans limit could be invalid at a low temperature even for millimeter wavelengths, we use the formula with the exponential terms of blackbody radiation:

$$\beta = \log\left(\frac{I_{\nu_1}}{I_{\nu_2}} \frac{\exp(h\nu_1/kT) - 1}{\exp(h\nu_2/kT) - 1}\right) / \log\left(\frac{\nu_1}{\nu_2}\right) - 3, \quad (1)$$

where I_ν is an intensity at a frequency ν , h is the Planck constant, k is the Boltzmann constant, and T is a temperature. We adopted an envelope temperature of 20 K, which is reasonable for a Class 0 YSO envelope and consistent with radiative transfer modeling (private communication with H.-F. Chiang). At a temperature of 20 K, the β value estimated using the Planck function is ~ 0.2 higher than that using the Rayleigh-Jeans approximation

in the 1.3 and 3 mm wavelengths. The original data of the $\lambda = 3$ mm continuum has a synthesized beam of $2''.1 \times 1''.8$ (PA = -74° , a position angle measured counterclockwise from north) as listed in Table 2. In order to compare with the $\lambda = 1.3$ mm continuum map and calculate the β map properly, we used a Gaussian-function tapering during map construction and achieved a beam of $2''.8 \times 2''.1$ (PA = -8°), which is nearly the same as the $\lambda = 1.3$ mm continuum map. The 1 mm and the tapered 3 mm continuum maps are shown in Figure 1 with the synthesized beams marked at the bottom right. The continuum peak measured by a 2D Gaussian function fitting is offset from the phase center to the southeast by $0.35''$ and is located at R.A. (J2000) = $20^h39^m06.26^s$ and Dec (J2000) = $+68^\circ02'15''.77$, which is consistent with higher angular resolution observations (e.g., Chiang et al. 2012).

The total continuum fluxes at $\lambda = 1.3$ and 3 mm in a central $10'' \times 10''$ box about the phase center are 0.472 ± 0.018 and 0.058 ± 0.002 Jy, respectively. Note that the absolute flux calibration uncertainties are not included. These continuum fluxes provide an estimate of circumstellar material mass (circumstellar disk and envelope, but mainly envelope mass) assuming the optically thin case (e.g., Looney et al. 2000): $M \approx F_\nu D^2 / \kappa_\nu B_\nu(T_d)$ (Hildebrand 1983), where F_ν is the integrated flux density, D is the distance to L1157 of 250 pc, κ_ν is the mass absorption coefficient, and $B_\nu(T_d)$ is the Planck function at dust temperature T_d . We assume κ_ν is $0.01 \text{ cm}^2 \text{ g}^{-1}$ at $\lambda = 1.3$ mm (Ossenkopf & Henning 1994), corresponding to ice mantle grains with a size distribution with a power of 3.5 (Mathis et al. 1977) and the typical gas-to-dust ratio of 100. Using a representative dust temperature of 20 K as addressed above, the envelope mass is $M_{env} \approx 0.583 \pm 0.022 M_\odot$, which is consistent with previous studies of radiative transfer modeling using a similar mass absorption coefficient (e.g., Kwon et al. 2009). Free-free emission of low-mass YSOs is minimal (at most a few percent) at millimeter wavelengths, and in the case of L1157 it is approximated at a negligible level of 0.5–0.7 mJy at $\lambda = 1$ to 3 mm (Tobin et al. 2013). Note that the mass estimate could be uncertain up to about a factor of two due to uncertain mass absorption coefficients. The mass estimate error is purely from the statistical error of the total fluxes: absolute flux calibration errors up to 15% (Section 2) is not included. In addition, we estimated the deconvolved sizes by Gaussian fitting: $2''.15 \times 1''.98$ (PA = -4°) and $1''.68 \times 1''.54$ (PA = -46°) at $\lambda = 1.3$ and 3 mm, respectively. The relatively more compact size detected at the longer millimeter wavelength suggests that the larger grains are centralized. The flux and size estimates at $\lambda = 3$ mm are made in the tapered map explained in the previous paragraph.

The right panel of Figure 1 shows how the derived dust opacity index, β , changes throughout the envelope of L1157 and is shown only at locations where both wavelength continua have a signal-to-noise higher than three. As shown in Figure 1, the central region of the envelope has a smaller β which is close to 0.3 (suggesting larger dust grains), and the boundary region has a large value around 2 (similar to those estimated in the interstellar

medium, implying small sub-micron grains). Note that β is most sensitive to the grain size (e.g., Draine 2006). This trend is understandable in the sense that grains grow fast in a dense central region, and the boundary has similar conditions to the interstellar medium, e.g., density and radiation field. The mean β , based on the total fluxes of the two frequencies, is 0.76. In addition we present both wavelength data and β with uv distances in Figure 2, which also shows a variation of β . We shifted the phase center to the continuum peak for the plot, and calculated β by Equation 1 assuming an optically thin case. In fact, β decreases with uv distance; the dense central region has a smaller β suggesting large grains. Large optical depth can also cause changes in β ; however, radiative transfer modeling could not explain such a large variation of β only with optical depth effects even in a more massive envelope object (Kwon et al. 2009). Indeed, although the uncertainties were large, data presented in Kwon et al. (2009) also show the same trend. In contrast, Chiang et al. (2012) did not detect such a variation of β for the envelope of L1157. We suspect that the discrepancy was caused by absolute flux calibration uncertainties, especially when Chiang et al. (2012) combined long baseline data taken in A and B configurations. In the common uv ranges, both data are in agreement within the absolute flux calibration uncertainties.

3.2. Molecular lines

In this section, we present the results of various molecular line observations toward the central envelope region with about $2''$ resolution. Figure 3 shows the integrated intensity maps of six molecular lines overlaid with the CO J=2–1 map¹. The blue- and red-shifted components of the central region of the outflow are shown in blue and red contours, respectively. Since the bipolar outflow is nearly on the plane of the sky ($i \approx 81^\circ$, Bachiller et al. 2001), the blue- and red-shifted components are clearly distinguished on opposite sides. In addition, the integrated intensity peaks are not located in the middle of both blue- and red-shifted lobes. Instead, they trace two edges in a conic shape.

The three CO isotopes are differently distributed. C¹⁷O J=2–1 shows a strong signal at the envelope and seems to trace the bipolar outflow edges, presumably entrained gas. In contrast, ¹³CO J=1–0 is detected toward the envelope and the CO bipolar outflow peaks. C¹⁸O J=1–0 does not trace the bipolar outflow and instead shows the envelope elongated perpendicular to the outflow. Interferometric observations suffer missing flux issues due to lack of short baselines. In the case of ¹³CO J=1–0, the brightness temperature of single dish

¹We indicate the rotational transitions only for CO and its isotopes. The spectral line details are found in Table 2.

observations is 6 K at the line profile peak (Gueth et al. 1997), which corresponds to about 16 Jy per single-dish beam of $22''$. As the total flux of our data over the same region is about 2 Jy, the missing flux is approximately 87%. As shown in Figure 5 and 6 of Gueth et al. (1997), however, the large missing flux is mostly due to the large-scale low level emission. Missing flux is small toward the central peak and narrow jet features. For C^{18}O J=1–0 and C^{17}O J=2–1, whose features are likely more compact, the missing flux is expected to be even smaller.

Differences among these three isotopes are also found in the line profiles. Figure 4 shows the six line profiles at their peak positions. ^{13}CO J=2–1, which arises from both the envelope and the bipolar outflow, has a self-absorption feature (or extended features filtered by the interferometric observations) and a broad wing component. C^{17}O J=2–1 and C^{18}O J=1–0 have narrow line profiles, and a Gaussian profile fitting gives a full width half maximum (FWHM) of 1.82 ± 0.19 and 1.13 ± 0.17 km s^{-1} , respectively. The hyperfine structures of C^{17}O span over about 1.8 MHz: 224.7135334, 224.7141870, 224.7147438, and 224.7153100 GHz (the Cologne Database for Molecular Spectroscopy, Müller et al. 2001). However, the lowest frequency line at 224.7135334 GHz is negligible since its integrated intensity is lower than the others up to by an order of magnitude. Therefore, the effective frequency span of the hyperfine structures would be about 1.1 MHz, which corresponds to about 1.47 km s^{-1} at the rest frequency. This explains the broad linewidth of C^{17}O : $\sqrt{1.47^2 + 1.13^2} \approx 1.85$ km s^{-1} . In Section 3.4, we will also show that there exists a velocity gradient for C^{17}O J=2–1 and C^{18}O J=1–0 about the envelope that may suggest rotation.

CS and CN also have clear detections. However, their peaks are located toward either the red- or blue-shifted outflow lobe. The peak of CS is north of the continuum center, which is toward the red-shifted outflow lobe, and the peak of CN is south, at the blue-shifted lobe. The line profile of CN has a FWHM of 0.73 ± 0.18 km s^{-1} and a velocity center of 2.1 ± 0.19 km s^{-1} . CN is the narrowest line presented in this paper and is found to be blue-shifted compared to the systemic velocity of 2.5 km s^{-1} . The CS line profile is very similar to C^{18}O in terms of the linewidth and the central velocity. However the angular resolution of the CS data is relatively poor, so the peak position is arguably consistent with the continuum peak. As the critical densities of the two transitions we detected are similar ($1.1\text{--}1.4 \times 10^6$ cm^{-3}), the discrepancy of CS and CN distributions may indicate the differences in formation and/or destruction. For example, CS and CN both trace bipolar outflows, but CN can be quickly destroyed, which results in a distribution closer to the heating source (e.g., Bachiller & Pérez Gutiérrez 1997). Note that single dish observations detected CS and CN over large regions of the bipolar outflow (e.g., Bachiller et al. 2001), but our observations are limited only toward the center.

The distribution of N_2H^+ clearly shows anti-correlation with CO. N_2H^+ is found in the outer region of the envelope with a hole at the center, and in the southeastern region adjacent to the blue-shifted outflow lobe.

This anti-correlation is well understood by the fact that N_2H^+ is destroyed by CO (e.g., Stephens et al. 2015). As shown in Figure 4, the line profiles of N_2H^+ around the east and west blobs marginally show multiple velocity components, as expected for infall features.

3.3. Infall of the outer envelope

Chiang et al. (2010) reported CARMA N_2H^+ observations with an angular resolution of $7''$ and found that the N_2H^+ traces well the flattened envelope structure Looney et al. (2007) detected in silhouette by *Spitzer*. They did not detect the central hole destroyed by CO at this angular resolution, but they did detect a double-peaked feature toward the central region with velocities around 2.7 and 3.1 km s^{-1} . They suggested that the two velocity components indicate infall motion. In addition, a feature supporting a solid body rotation in a large scale of ~ 20000 AU was reported, which was argued as inherited from the large filamentary or flattened envelope kinematics.

Our interferometric data with an angular resolution of $\sim 2''$ are not sensitive to the large scales of ~ 20000 AU, so the component interpreted as a solid body rotation by Chiang et al. (2010) is filtered out. We convolved our N_2H^+ channel maps with the identical synthesized beam of Chiang et al. and compared the $JF_1F = 101 \rightarrow 012$ hyperfine components (i.e., the more isolated hyperfine component in the N_2H^+ spectra, located at a $V_{LSR} \sim -6.5$ km s^{-1} in Figure 4). We found that the line profile peak of our data is about 0.7 Jy beam^{-1} while Chiang et al. obtained 0.9 Jy beam^{-1} , which implies that our observations filters out $\sim 22\%$ of the N_2H^+ flux observed by Chiang et al. Despite the missing flux and poor sensitivity of our data, two velocity components are marginally detected toward each of the east and west blobs. For each blob, individual N_2H^+ spectra were fit with two sets of Gaussian velocity components. The 7 hyperfine structures were fit simultaneously; their rest frequencies and relative strengths are adopted from Caselli et al. (1995) and Womack et al. (1992), respectively. Since the sensitivity is marginal, we simply assumed optically thin emission and local thermal equilibrium. In addition, it is assumed that the two velocity components have the same linewidth. The fits results in velocity components of 2.6 ± 0.04 and 3.0 ± 0.06 km s^{-1} for the west blob and 2.5 ± 0.07 and 3.1 ± 0.09 km s^{-1} for the east (Figure 5). The FWHM is 0.4 ± 0.06 km s^{-1} in the west blob and 0.6 ± 0.11 km s^{-1} in the east blob. The reported errors are statistical fitting uncertainties. Note that the spectra used for the fitting have a velocity resolution of 0.1 km s^{-1} . N_2H^+ is known to be

optically thin for L1157, so the double peaks are unlikely due to a self-absorption feature. Due to the low signal-to-noise at high spectral resolution, we also investigate whether a single velocity component can fit the data. The reduced χ^2 value for the single velocity fit is almost identical to the two velocity fit. However, the line profiles show obvious signs of two velocity components, particularly for the isolated, $JF_1F = 101 \rightarrow 012$ hyperfine component (Figure 5), suggesting two velocity components may be meaningful.

These two velocities are consistent with previous studies of lower angular resolutions discussing infall motion (e.g., Chiang et al. 2010). Since the two blobs present similar double velocity components rather than a velocity gradient, the outer envelope (~ 1000 AU scale) detected in our N_2H^+ data is thought to be dominated by infall motion. The inner region of the N_2H^+ hole is nicely imaged with CO isotopes and consistent with a rotation feature (Section 3.4). The outside wall of the bipolar outflow cavity is also traced by N_2H^+ in more compact configurations (Chiang et al. 2010; Tobin et al. 2012). Hereafter, we will refer to the outer envelope as the region traced by N_2H^+ from 500 to 1000 AU, and the inner envelope as the region traced by C^{18}O . Note that the dust continuum traces both these envelope scales. The outer envelope, as mapped by Chiang et al. (2010), extends to ~ 20000 AU scales, but again the observations in this paper cannot detect this large-scale structure due to spatial filtering of the interferometer.

3.4. Rotation of the inner envelope

As shown in Figure 3, CO isotopes well trace the envelope structure. In particular C^{18}O presents an elongated feature perpendicular to the bipolar outflow. In order to investigate the kinematics of the inner envelope, we examined the position-velocity (PV) diagrams of C^{17}O and C^{18}O cut through the phase center along two directions: the bipolar outflow ($\text{PA} = 140^\circ$) and the elongated envelope (70°). The PV diagrams along the elongated envelope feature show a velocity gradient, while the cut along the bipolar outflow does not. The left and right panels of Figure 6 present the C^{17}O and C^{18}O PV diagrams cut in the elongated envelope. C^{17}O shows double peaks in the PV diagram with a positional offset. This feature is not due to the hyperfine structures of C^{17}O . Unresolved hyperfine lines produce broader linewidths (Section 3.2), and resolved hyperfine lines may show multiple peaks but not a velocity gradient. The velocity gradient corresponds to 1.1 km s^{-1} over $0''.7$ or 180 AU at the target distance of 250 pc.

The C^{18}O features are relatively complicated, but the signals are mainly located in the top right and bottom left in the diagram, which means that the eastern part of the elongated envelope is redshifted and the western part is blueshifted. This overall velocity gradient is in

agreement with C¹⁷O. Note that the green lines in the two panels connect the same locations in position and velocity. The features shown in both C¹⁸O and C¹⁷O could be a rotation, which is clockwise when looking down from the north. The 3.1 km s^{−1} component detected around an offset of −2'' is at the boundary of the outer envelope traced by N₂H⁺, suggesting this could be infalling material.

The mass of the central objects can be estimated from the rotational features of the molecular lines. Although our data are not high enough quality for clear evidence of Keplerian rotation, it is worthy to estimate the central object mass based on the interpretation. In Figure 6 we also overlaid Keplerian rotation curves of a central protostar with a mass of 0.04 and 0.02 M_{\odot} with blue and orange lines, respectively. The mass of 0.04 M_{\odot} matches the overall outline of the C¹⁸O features in the PV diagram and the velocity gradients detected in both C¹⁸O and C¹⁷O. The mass of 0.02 M_{\odot} is marked to show how much the curve changes with mass. The bipolar outflow is known to be nearly in the plane of the sky, which presumably suggests that the rotation feature is close to edge-on. Nevertheless, we show two dashed lines for the cases of 60° inclination from the plane of the sky. The 60° inclination line is equivalent to half the rotational velocities at a given radius. In other words, if the distance were indeed a half of 250 pc, the edge-on case is shown by the dashed lines. Similarly, the opposite case of a 500 pc distance can simply be estimated in the plot.

For the Keplerian rotation curves, we did not take into account the envelope mass within a given radius: $M(R) \approx M_{env}(R/R_{out})^{3-p}$, where M_{env} is the total envelope mass (0.58 M_{\odot} , as derived in Section 3.1), R_{out} is the envelope size (5''), and p is the power-law index of a volume density distribution. When assuming $p = 1.8$ (Kwon et al. 2009), the envelope mass inside 0''.35 (the radius of the offset between the two peaks in the PV diagrams connected by a green line in Figure 6) is 0.02 M_{\odot} . Due to the cavity swept by the bipolar outflow and the sharply increasing dust temperature close to the center, the mass inside is likely smaller than this estimate. This implies that Keplerian rotation tends to appear inside around 0''.35 where the envelope mass portion can be neglected, while a “constant” velocity might appear beyond 0''.55 (~ 140 AU at a distance of 250 pc) where the envelope mass inside is comparable to the protostellar mass (0.04 M_{\odot}): $v = (GM(R)/R)^{1/2}$, i.e., $v \propto R^{2-p}$. Again, on the scales of 1000 AU, infall motion is detected in N₂H⁺.

Although it is not clear due to the limitation of our data in sensitivity and resolution, Figure 6 indicates that the outer contours and the overall gradient in the green line can be explained by Keplerian rotation around a 0.04 M_{\odot} protostar. Note that we adopted the distance of 250 pc, which is most reasonable (Looney et al. 2007), but the mass estimate decreases or increases linearly depending on the distance. Gueth et al. (1997) estimated the central protostellar mass as 0.2 M_{\odot} based on the velocity gradient detected in C¹⁸O, but

they assumed the distance of 480 pc and overestimated the interval across the 1 km s^{-1} velocity gradient roughly as $\sim 3''$, which both cause an overestimate of the protostellar mass. Since Gueth et al. (1997) interferometric observations have a comparable angular resolution to our data, missing flux might not cause a significant bias. It is not easy to compare the two interferometric data sets since they have different channel widths and a weighting. Their Figure 9 presents a channel map with uniform weighting and shows intensity peaks separated by $3''$, but the span only appears well in two adjacent channels (2.81 and 3.02 km/s), not blue- and red-shifted channels. On the other hand, their Figure 4 that uses a natural weighting shows a similar position span for the velocities we observed. Considering the uncertainties and differences of both data sets, we argue that our interpretation is not so problematic, and that the two estimates are consistent. Based on the dust continuum, we estimated the envelope mass as $\sim 0.58 M_{\odot}$ (Section 3.1), which gives an envelope to protostellar mass ratio of about 14.

4. Bipolar outflow

4.1. Outflow activity

The left panel of Figure 7 shows the CO emission integrated in velocity (moment 0) observed in the E-array configuration (black contours) at a $5''$ spatial resolution overlaid on the $8 \mu\text{m}$ emission taken by the *Spitzer* telescope (Looney et al. 2007). The figure clearly shows overlap of the $8 \mu\text{m}$ and CO emission. Note that the *Spitzer* $8 \mu\text{m}$ channel may be dominated by H_2 0–0 S(5) and S(4) tracing shocked gas (Looney et al. 2007). The CO emission indicates a wiggling bipolar morphology running northwest-southeast, which is a well-known indication of precession that is also detected in several low energy SiO transitions (e.g., Zhang et al. 2000). Within about $30''$ from the central protostar, the CO emission shows a point symmetric X-shape morphology composed of two narrow ridges of $\sim 3''$ width. At further distances, the CO emission consists of several bright knots along an elongated curved structure spanning in total $\sim 300''$ (75000 AU). Most of the bright knots have been extensively reported and studied in the past (e.g., Bachiller et al. 2001), including B0, B1 and B2 in the blue-shifted (southern) lobe and R, R0, R1 and R2 in the red-shifted (northern) lobe as indicated in Figure 7.

The upper right panel of Figure 7 is a zoom-in of the central region, showing contours of the CO emission observed in CARMA D configuration at $2''.5$ resolution. The color scale once again shows the *Spitzer* $8 \mu\text{m}$ emission and the yellow tones indicate the well-known extinction lane perpendicular to the outflow. The observations show a clear X-shape pattern, with the strongest emission in the northwest and southeast arms. The average FWHM of

these arms is about $3''.3$, which is about $2''.2$ (550 AU) in width after deconvolving with the beam. The lower right panel of Figure 7 shows the CO centroid velocity (moment 1) map of the central region. The velocity in this map ranges from -7.5 km s^{-1} to $+12.5 \text{ km s}^{-1}$ (note that the velocity is indicated with respect to the cloud velocity $V_{LSR} = +2.6 \text{ km s}^{-1}$, section 3.4). By inspecting the image, it is evident that close to L1157-mm, the northwest-southeast arm of the X-shaped structure has an average absolute velocity $2\text{--}3 \text{ km s}^{-1}$ higher than the northeast-southwest arm. The arms of this X-shaped emission has been interpreted as the limb-brightened cavity walls of the outflow (e.g., Gueth et al. 1997; Gómez-Ruiz et al. 2013). However, our data show certain similarities between the northwest and southeast arms in morphology, symmetry, brightness, and kinematics of the emission, suggesting components of one jet. The same occurs with the northeast-southwest arms, though fainter, suggesting these arms could be another jet. In Section 4.2 we discuss the possibility that the CO emission is associated with multiple outflows or molecular jet ejections from the central disk-protostar system.

Even though CARMA is filtering out the fainter emission between the two bright narrow ridges shown by the single-dish and interferometer combined CO J=1–0 map of Gueth et al. (1996), which interpreted the system as a limb-brightened cavity, the possibility of two jets is not ruled out. Gueth et al. (1996) reported a very high emission contrast between the ridges and the region enclosed by the ridges, which they could not completely model even using an exponential decay in the density profile of the putative cavity. The compactness of ridges allows CARMA to detect them: the largest angular scale of CARMA in this configuration goes up to $\sim 20''$. The proposed multi-jet model does not need to recover all the extended flux to be tested and has the advantage of explaining several observed features that cannot be explained by the cavity model. As mentioned in Gueth et al. (1996), the cavity model has a difficulty in explaining (1) the edge-inner cavity emission contrast, (2) the morphology of the emission at high velocity showing only the cavity walls, and (3) the non-homogeneous emission of the inner cavity showing several arches and small filaments.

Figure 8 shows the CO emission integrated over 6 arbitrarily selected velocity intervals so that the overall morphology and kinematics of the outflow are adequately depicted. The extended emission at velocities close to the systemic velocity is filtered by the interferometer and hence not shown. Although the rest of the velocity channels are also affected by the presence of extended emission, the main issue is the dynamic range of the images since the narrow outflow ridges are much brighter than the emission from the putative inner cavity material (Gueth et al. 1996). Nevertheless, we have checked that the sidelobes have little impact in the brightness distribution of the ridges themselves. We also noticed in the CO moment 0 image, there are some artifacts at the edges of the images. In particular, the emission features west of R1 and R0 and west and east of B1 are sidelobes of the strongest

outflow ridge. These edge problems only appear in the channels (Fig. 8) where this ridge is stronger. On the contrary, the emission southeast of R1 is clearly not an artifact. One can see for instance, that its curvature is the opposite from the main northwest ridge passing through R0.

The redshifted high velocity CO emission ($+16.2, +32.0 \text{ km s}^{-1}$; Fig. 8 a) traces part of the northwest outflow lobe with some finger-like features protruding northwest from the curved molecular jet path. At medium velocity ($+9.6, +15.7 \text{ km s}^{-1}$; Fig. 8 b) the CO emission runs mainly from the protostar position and extends northward to knot R along a western curved ridge. There is also emission along the eastern curved feature southeast of R1, although this feature was not well mapped due to the limited field of view of our observations. Some emission is also detected north of knot R. The redshifted low velocity emission ($+4.0, +9.1 \text{ km s}^{-1}$; Fig. 8 c) is similar to that of the medium velocity emission. The emission runs outward from the protostar along the knots R0, R1, R, and R2. CO emission is also seen northeast of L1157-mm and southeast of R1 which may indicate a different curved jet path. This velocity channel shows emission at knots R and R2. Also evident is that the curved features cross each other at the infrared knots R and R1. Close to the cloud velocity ($+1.5, +3.5 \text{ km s}^{-1}$; Fig. 8 d), the emission associated with knots R0 and R1 becomes fainter, while that at knot B2 in the southern blue lobe becomes obvious. For the blueshifted low velocity ($-2.0, -0.5 \text{ km s}^{-1}$; Fig. 8 e), knot B2 shows an extended morphology. Hints of arched structures apparently crossing each other are seen at B1 and B2. At both low and high blueshifted velocities, the main southeast curved ridge is seen from L1157-mm and along knots B0 and B1. In addition, there is a blueshifted emission component in the middle of the northern lobe at $\sim 60''$ north of L1157-mm. At high blueshifted velocities ($-19.8, -2.6 \text{ km s}^{-1}$; Fig. 8 f), an arch joining L1157-mm with the western part of B1 forms the southwest curved ridge.

We do not include velocity dispersion (second moment) maps in this paper because the spectral profiles of the CO emission show extended emission wings that appear masked by the core emission of the line profiles. Pronounced wings (extending up to $\sim 33 \text{ km s}^{-1}$) are commonly found along all the knots marked in Fig. 7, while the rest of the gas have linewidths between $(1-3) \text{ km s}^{-1}$.

Figure 9 shows a zoom-in of the north lobe of the outflow. It shows the infrared $8 \mu\text{m}$ emission overlaid with the CO redshifted high velocity emission between $+32 \text{ km s}^{-1}$ and $+18 \text{ km s}^{-1}$. This image shows two clear finger-like features at $140''$ and $150''$ from the L1157-mm position at a PA of -60° and -50° respectively. There is also possibly a third finger at $155''$ away from L1157-mm at $\text{PA} = -40^\circ$. The tip of these fingers spatially coincide with some of the mid-IR knots studied by Takami et al. (2011). All three features are marked

in the figure with a straight line joining each of them with the position of L1157-mm. Their linear trajectory along with their high velocity suggests that they can be molecular bullets ejected with different position angles. Therefore, these fingers indicate a possible rotation and precession of the ejecting source.

4.2. Two molecular jets in L1157

Previous work based on molecular observations towards L1157 (Gueth et al. 1996, 1998; Bachiller & Pérez Gutiérrez 1997) have proposed the existence of an episodic precessing jet which drags the environment and excavates a wide cavity. The cavity walls are limb-brightened and hence easily detected in molecular emission. However, the L1157 outflow shows a point reflection symmetry of the strongest clumps at the northwest and southeast putative cavity walls. The symmetry of the walls is seen via three physical parameters: shape, radial velocity, and clump structure. Thus, previous investigations (Zhang et al. 2000; Bachiller et al. 2001) indicated the possibility that not only the CO emission but also the SiO emission (a well known tracer of the shocked gas in molecular outflows and jets) in L1157 is tracing one narrow molecular precessing jet, coincident with the northwest-southeast CO arm seen close to the protostar. The idea of a precessing jet is reinforced by the finding of high velocity shocks at different position angles in the north lobe of the outflow (see Section 4.1). Bachiller et al. (2001) also speculated the existence of a milder wide-angle wind surrounding this narrow precessing jet, which would account for the weak CO molecular emission (undetected in SiO) to the northeast of the red (northern) lobe and the southwest of the blue (southern) lobe. However, this scenario can poorly account for this “anomalous” emission since it is not detected at both sides of the outflow simultaneously (i.e., there is no CO emission west of the narrow SiO molecular jet in the north lobe and to the east in the south lobe). Moreover, the velocity of a wide-open angle wind is expected to decrease with the opening angle from the outflow axis (Arce & Sargent 2004). However, such a characteristic is not found in our data.

On the basis of the new CARMA CO observations, we explore the possibility of the ejection of multiple jets from the L1157 protostar. In particular we fit a two precession jet model to the CO data. The idea of a precessing jet needs a mechanism to eject material that follows ballistic trajectories. Evidence for high velocity ballistic ejections are clearly shown in Figure 9. In addition, there is evidence suggesting that some of these bullets are cometary-shaped and run parallel to each other in the southern lobe (Takami et al. 2011). This matches well with the idea of multiple jets or ejections being present in the outflow.

We suggest that the initially supposed limb-brightened cavity edges (e.g., Gueth et al.

1996, 1998) can possibly be the path of two molecular jets (see Figure 10 for a sketch of this new interpretation). The CO CARMA images (Figures 7 and 8) show a clear wiggling path running northwest-southeast close to the central protostar. It coincides well with the previously identified SiO molecular jet, which we call *Jet 1*. The CO emission shows also another S-shaped feature running northeast-southwest close to the protostar which we call *Jet 2*. *Jet 2* shares similar physical characteristics with *Jet 1*: (1) a sinuous trajectory, (2) a similar physical width and length, (3) a similar linewidth of the line core, and (4) a point reflection symmetry that is especially clear at the center of the system (Figure 7). However, the radial velocity of *Jet 2* is closer to the systemic velocity than for *Jet 1*. Another difference is that *Jet 1* shows in general, lines with more extended wings than *Jet 2*.

In Section 4.3, we present a numerical fit to the L1157 CO outflow based on a two precessing molecular jet model, which is in contrast to the wide-angle wind scenario. We propose this modeling as a proof of feasibility of a multiple jet model, although this kind of system has been recently proposed for another Class 0 object, NGC 1333 IRAS 4A2 (Soker & McIcley 2013). In that case, the authors tried to explain the observed velocity gradient in the gas of the outflow (Choi et al. 2011), which is perpendicular to the outflow axis as produced by the ejection of multiple jets.

In the two molecular jet scenario, the jets can be launched at the same time or at different epochs. A system simultaneously ejecting two jets may be possible if there are two protostars ejecting two corresponding jets (Murphy et al. 2008). A striking example of a binary system (or triple) in which both protostars are launching bipolar precessing ionized jets is L1551 IRS 5 (Rodríguez et al. 2003; Pyo et al. 2009; Lim & Takakuwa 2006; Itoh et al. 2000; Fridlund & Liseau 1998). This system has a separation of 45 AU between the two circumstellar disks, each of 10 AU in radius. Recent VLA observations of L1157 (Tobin et al. 2013) have shown a compact although somewhat elongated disk-like structure with a radius of ~ 15 AU, indicating that only one protostar is present in the system at a 12 AU resolution. On the other hand, a re-evaluation of the same data with a weighting more sensitive to find structures (i.e., $\text{robust} = 0$) suggests that there could be a binary system with ~ 15 AU separation (J. Tobin, private communication). At this time, we cannot determine if L1157 is a close binary system or not.

In the case that L1157 is a single protostellar system, the two molecular jets could be ejected at different times, which could explain why the CO emission of *Jet 2* is weaker than that of *Jet 1* and why *Jet 2* does not show SiO emission (thought to disappear in older and slower shocks, see e.g., Codella et al. 1999; Miettinen et al. 2006; Fernández-López et al. 2013). Thus, *Jet 2* would be a remnant of an older ejection that entrained the molecular environment. Although L1551 IRS 5 observations support the scenario of two jets, there

is one noticeable difference between the system and L1157. The former has jets with a markedly dissimilar radial velocity (separated by $\sim 140 \text{ km s}^{-1}$), possibly indicating two well separated ejection axes, while in L1157 the two jets show similar radial velocities, which may indicate similar ejection axes with only a small inclination difference. This axis would be inclined differently which may be due to secular motions of the system itself. On the other hand, there could be different ejection mechanisms launching multiple jets simultaneously, e.g., a circumstellar disk with an accreting spiral pattern of multiple arms launching a jet each (see Soker & McIey 2013). This discussion lies beyond the scope of this paper.

4.3. 3D model fitting to the CO emission

As stated in the previous section, we suggest that L1157 may be ejecting two precessing bipolar jets, which we called *Jet 1* and *Jet 2*. For each jet, we fit the data using a precessing jet model put forward in Raga et al. (2009). This model consists of a jet launched by a disk-protostar system with a precession determined by half the opening angle (α) and a characteristic frequency, ω . The bipolar jet is affected by the precession of the launching system and ejects material running into ballistic trajectories with constant velocity, v_j . For this analysis, we did not consider additional perturbations due to an orbital binary motion since we do not know if L1157 is a binary system and this kind of perturbation displays a pattern only discernible at smaller spatial scales (Raga et al. 2009). In our model, the ejecta shows a helix-like geometry in which the radius of the helix gets wider with time. The following equations, as derived from Raga et al. (2009), describe the outflow motion in a reference frame centered in the disk-protostar system (see Figure 2 in Raga et al. 2009):

$$\begin{pmatrix} x \\ y \\ z \end{pmatrix} = (t - \tau) \begin{pmatrix} v_x \\ v_y \\ v_z \end{pmatrix}, \quad (2)$$

where the velocity of the ejection is

$$\begin{pmatrix} v_x \\ v_y \\ v_z \end{pmatrix} = v_j \begin{pmatrix} \sin \alpha \cos (s_{prec} \omega \tau - \phi_0) \\ -\sin \alpha \sin (s_{prec} \omega \tau - \phi_0) \\ \cos \alpha \end{pmatrix}. \quad (3)$$

In these equations, t is the present time and τ is the “negative” time at which a parcel of the jet was launched such that $t = 0$ means “now”. s_{prec} defines the direction of rotation with +1 indicating clockwise (when seen from top of the Dec axis) and –1 indicating counter-clockwise rotation. ϕ_0 is the phase angle in the xy-plane of the current ejection at $\tau = 0$.

Also we allow a possible inclination angle i with respect to the sky plane and a position angle, pa , defined counter-clockwise from north. Thus, we doubly rotate the *jet system* in xyz coordinates to get the *plane of the sky* $x''y''z''$ coordinates, where x'' is in the RA direction pointing west, z'' is in the Dec direction toward north and y'' is perpendicular to the plane of the sky, pointing away from us. Given the data provided by the observations (x'' , z'' , and v_y'') and assuming the velocity of the ejection does not change, one can obtain the ejection time τ for each data-point using:

$$\tau = -\sqrt{\frac{(x'')^2 + (z'')^2}{v_j^2 - (v_y'')^2}}. \quad (4)$$

As can be seen from the parametric equations above, τ can be used as the *parameter*, to derive a synthetic model, once a set of free variables (s_{prec} , v_j independent for each jet lobe, α , ω , i , pa , and ϕ_0) is determined. This can be used to speed-up the fitting process.

With the model at hand, we extracted the information on position (x'' , z'') and radial velocity (v_y'') of the molecular emission for each jet by picking out points of peak emission from each 2.5 km s^{-1} binned velocity channel image. All the selected points were above 3σ and followed an arbitrarily designed jet path. After repeating the data selection process several times for each jet, the final *Jet 1* and *Jet 2* data points were defined (Figure 11). Figures 11, 12, and 13 show the radial velocity and trajectories of the model compared with the observed data. As can be seen from these figures, there is good position and kinematic agreement between model and data. Table 3 shows the values obtained in fitting the two jets. The model gives higher velocities for the northern lobes ($60\text{--}90 \text{ km s}^{-1}$) than for the southern lobes ($30\text{--}40 \text{ km s}^{-1}$) in both jets, which may be expected since the northern lobe extends farther than the southern lobe. This could imply, for instance, that different lobes are ejected at different intrinsic velocities or with different inclination angles. We choose our model to have two independent velocities for each north-going jet and south-going counter-jet. The CO may be tracing the jet directly ejected from the surroundings of the central star, or material swept up by the jet just in the surroundings of the bullet path, making possible differences between the intrinsic velocity in the jet and counter-jet. On the other hand, the CO emission may be tracing the material swept up by the jet far from the bullet path. In this case, Bachiller et al. (2001) proposed that the environment surrounding the southern lobe is denser than that surrounding the northern lobe, thereby reducing more efficiently the velocity of the southern lobe. Our model shows also an agreement between the precessing period of the jets (derived from the model, they are about $T = 5000\text{--}8000$ years) and their precessing angles (11°). However, the position and inclination angles are different for both jets, suggesting a slightly different ejection axis orientation. The fact that the period and precessing angle of both *Jet 1* and *Jet 2* are similar could support the scenario of the two jets

ejected at different times described in Section 4.2. In such a case, one problem is to explain the different ejection axis orientation that we previously explained as secular motions of the system itself. Such a problem may simply be explained by two protostars each ejecting an outflow.

A note of caution should be made here in establishing that our fitting is aimed uniquely to probe the feasibility of a two precessing bipolar jet model in order to explain the observed L1157 CO emission. We have not tried to univocally fit the model to the data in any case, and we are aware that other models with multiple jets could fit the data as well. For instance, *Jet 2* has a solution with $s_{prec} = -1$ as good as the one with $s_{prec} = 1$ shown here. This is probably due to the poor sampling of *Jet 2* in the north lobe and also because the relative weakness of its CO emission compared to that of *Jet 1*. We choose not to show the solution with $s_{prec} = -1$ here for consistency on the direction of precession with *Jet 1* which has s_{prec} very well constrained. Again, even though the model can be regarded as somewhat arbitrary, its purpose is to qualitatively show the possibility that the system is composed by at least two precessing molecular jets and to provide an order of magnitude estimates of the physical parameters.

5. Discussion

5.1. Possible causes of precession in L1157

The cause of the wiggling (precession) pattern of the protostellar jets is not well known. There are theoretical models explaining this phenomenon as caused by (1) the orbital motion of a binary system (e.g., Masciadri & Raga 2002), (2) the precession due to the tidal interaction between the disk of one protostar and a companion protostar in a non-coplanar orbit (e.g., Terquem et al. 1999a; Montgomery 2009), (3) the warp of the inner disk (in principle caused by a perturbing companion star) from which the jet is thought to be launched, and/or (4) the misalignment between the disk rotation axis and the ejection engine, with the latter usually understood as an MHD disk-wind (Frank et al. 2014). At this moment there is no conclusive empirical evidence supporting any of these scenarios. The first three models would imply a multiple (at least binary) protostellar system, while model (4) would just require a single protostar. Nonetheless, in many (if not all) of the protostellar systems with observed precessing jets, evidence indicate that they are mostly binary systems (e.g., HH30, Guilloteau et al. 2008; HH211, Lee et al. 2010; H111, Reipurth et al. 1999), and hence we do not explore the model of the jet launching engine misaligned with the disk rotation axis, although we note that it should remain as an alternative mechanism. We rule out the orbital motion model because it entails a mirror symmetry for the jet, a small outflow

opening angle, and a very short period spiraling outflow (Raga et al. 2009), all of which are not observed in our data. We cannot test the possibility of a warped inner disk since we do not have observational data of the dust emission at AU scales. We thus test the tidal precession model with the L1157 jets. The tidal precession model has a good theoretical background that we use to derive the orbital parameters of a hypothetical binary system producing the precession of the jets. In particular, we use an equivalent form of equation (37) from Montgomery (2009) for circular precessing Keplerian disks. This equation relates the angular velocity at the disk edge (ω_d), the Keplerian orbital angular velocity of the companion around the primary protostar (ω_o), and the retrograde precession rate of the disk and the jet (ω_p):

$$\omega_p = -\frac{15}{32} \frac{\omega_o^2}{\omega_d} \cos \alpha \quad , \quad (5)$$

where α is the inclination of the orbit of the companion with respect to the plane of the disk (or obliquity angle), and this angle is the same as the half-opening angle in equation 3 (Terquem et al. 1999b). The equation also assumes that both objects of the binary system have the same mass. Introducing the values for the jet precessing angle α and the precession period τ_p derived from our fit (Table 3) and adopting some reasonable value for the radius of the disk r_d responsible for launching the jet, we can constrain the orbital period τ_o and the orbital radius r_o of the putative binary system. Tobin et al. (2013) showed that the disk radius is less than 15 AU, and we take 1 AU as a lower limit for it. From this we derived orbital periods and radii in terms of the primary and secondary protostar’s solar masses, M_1 and M_2 : here $M_1 = M_2$. For *Jet 1* the orbital period is (50–370) $M_1^{-1/4}$ yr, while for *Jet 2* the orbital period is (60–450) $M_1^{-1/4}$ yr. The orbital radius for *Jet 1* is (13–52) $M_1^{1/3}$ AU and for *Jet 2* the orbital radius is (15–60) $M_1^{1/3}$ AU. It is evident that there is a good agreement between the τ_o and r_o estimates for *Jet 1* and *Jet 2*, as expected from the similar precession periods and angles, and intrinsic velocities. Moreover, the derived orbital radius is consistent with being a few times the disk radius which is expected for disks affected by tidal truncation (e.g., Artymowicz 1994). Indeed, using the derived mass of $0.04 M_\odot$ for the protostars (Section 3.4, $M_1 = M_2 = 0.02 M_\odot$), we then obtain $\tau_o = 130$ –1200 yr and $r_o = 7$ –31 AU for a disk with $r_d = 1$ –15 AU.

5.2. Understanding the bipolar outflow kinematics with the envelope

The precession direction that our models prefer is clockwise when looking down from north ($s_{prec} = +1$, Table 3). Since precession due to tidal interaction of a companion in a non-coplanar orbit occurs in the opposite direction to the rotation of the disk (the so-called retrograde precession), the outflow launching structure would rotate counter-clockwise.

However, our C^{18}O and C^{17}O data show a clockwise rotation of the inner envelope (eastern side redshifted). This implies the disk and the inner envelope would be counter-rotating. We discuss how to understand this counter-rotation of the inner envelope and the outflow launching structure and the caveats. When discussing the launching structure, we specifically mean protostars of a binary system or a circumbinary/circumstellar disk.

The precession direction of *Jet 1* is significantly well constrained. In contrast, *Jet 2* direction is relatively unclear: the clockwise and counter-clockwise cases are comparable in our modeling. This is probably due to the fact that *Jet 2* is not as strong as *Jet 1*. It is unrealistic to assume that the two jets are precessing in opposite directions. Therefore, we did not consider this case. On the other hand, the inner envelope rotation features discussed with our C^{18}O and C^{17}O data are also not decisive due to lack of angular resolution: the velocity gradient could be contaminated by the bipolar outflow. The possibility is low, however, as the profiles are along the elongated direction nearly perpendicular to the bipolar outflow, and the same directional velocity gradient in the inner envelope was also reported by Gueth et al. (1997). Based on the argument above, the counter-rotation of the inner envelope and the jet launching structure could be accepted.

Such counter-rotation does not seem to be realistic in terms of angular momentum in star forming molecular core scales. However, some planets and moons show counter-rotating motions in the solar system and counter-rotating binary systems may be theoretically feasible, for instance, as a result of the interactions of a triple system (Li et al. 2014). In addition, the kinematics of the L1157 flattened envelope are complicated. The large-scale solid body rotation detected in N_2H^+ by Chiang et al. (2010) is counter-clockwise, while their intensity weighted velocity map shows an overall direction switch at a smaller scale (Figure 3 in Chiang et al. 2010). Counter-rotation indeed helps a circumbinary disk last longer and is more effective during the binary system eccentricity evolution (Dunhill et al. 2014). It is not known yet, but L1157 might be a close binary system at 15 AU scale (J. Tobin, private communication). Although it is not ideal in the viewpoints of angular momentum, the binary protostellar system and the circumbinary disk could be counter-rotating. However, the detailed studies on how such a counter-rotating system forms is beyond the scope of this paper.

On the other hand, the modeling formalism we used is identical to a rotation case, so it is possible to interpret the modeling results as a clockwise rotation instead of precession. However, the periods of several thousand years that our models constrain are too large for a reasonable launching radius. Assuming Keplerian rotation around the protostar, the periods give a 70–80 AU launching radius.

Finally, the jet modeling formalism we used could also be applied to the precession of a

misaligned launching structure with respect to the system rotation axis (like the mentioned case 4 on previous section 5.1), so it is possible to interpret the modeling results as a prograde rather than a retrograde precession. A prograde precession is also expected in the case of a warped inner disk. Higher angular resolution and better sensitivity observations will provide decisive kinematic results toward this interesting Class 0 protostellar system whose bipolar outflow launching structure appears to be rotating in the opposite direction of the inner envelope.

6. Conclusions

We present CARMA millimeter observations of the youngest Class 0 protostellar system L1157. The central envelope region (L1157-mm) was imaged in $\lambda = 1.3$ and 3 mm continua, CO, C¹⁷O, CS, CN, ¹³CO, C¹⁸O, and N₂H⁺ with 2'' resolution. We also observed CH₃OH, H₂O, SO, and SO₂, but these lines were undetected with the sensitivity of these observations. The continua and the various line features allow us to estimate the physical properties of the envelope. In addition, we obtained a large (5') mosaic image covering the bipolar outflow of L1157 in CO J=2–1 with 5'' resolution. Our results are summarized in the following:

1. The envelope mass based on the dust continuum flux is estimated to be $\sim 0.583 \pm 0.022 M_{\odot}$. We also found that the dust opacity spectral index β changes along radius in the image, which is also shown in the visibility data.

2. Among CO isotopes, ¹³CO traces the CO peaks of the bipolar outflow, while C¹⁷O traces the edges. C¹⁸O shows a structure elongated and perpendicular to the bipolar outflow on the scale of 100 AU (i.e., it may be tracing the inner envelope). We also detected a velocity gradient in C¹⁷O and C¹⁸O, which is consistent with Keplerian rotation around a protostar with a mass of $\sim 0.04 M_{\odot}$ (approximately 1/14 of the envelope mass). The envelope is rotating clockwise when looking down from the north.

3. N₂H⁺ presents double peaks in east-west along the known flattened envelope direction with a hole at the center. Each of the double peaks shows a line profile understood by two velocity components, which suggests infall motion in the outer envelope of 1000 AU scales.

4. From the bipolar outflow mosaic image in CO, we detected several ballistic ejections in the redshifted (northern) outflow that support multiple jets. We find that the bipolar outflow could be interpreted as two jets for a reliable example, and we constrain this scenario by modeling the data cube. The idea of two jets is supported by the following observational evidence.

i. The morphology of the CO emission agrees with the two jet scenario. High-angular resolution CO data show two apparent collimated molecular jets in an X-shape distribution close to the protostar. In addition, the curved features at large-scale are well reproduced by the precessing two jet model.

ii. The CO brightness distribution is not well explained by single outflow cavity models but can be explained by the two jet scenario. The two jet scenario can explain the brightness asymmetry between the NW-SE ridge and the NE-SW ridge. The two jet scenario also can explain the large brightness contrast between the edges and inner part of the lobes.

iii. The radial velocity of the NW-SE jet gas is $2 - 3 \text{ km s}^{-1}$ higher than the NE-SW jet gas, which is unexpected for a single jet. Our model of two precessing jets can explain the different radial velocities, as well as positions, of the NW-SE and NE-SW jets.

iv. The spatial distribution of the SiO emission, which has been observed in the NW-SE jet but not in the NE-SW jet (Bachiller et al. 2001), can be explained if these two jets have different ages.

We are grateful to CARMA staff and observers for their dedicated work and anonymous referee for valuable comments that allowed us to improve the paper significantly. Support for CARMA construction was derived from the states of Illinois, California, and Maryland, the James S. McDonnell Foundation, the Gordon and Betty Moore Foundation, the Kenneth T. and Eileen L. Norris Foundation, the University of Chicago, the Associates of the California Institute of Technology, and the National Science Foundation (NSF). Ongoing CARMA development and operations are supported by NSF under a cooperative agreement, and by the CARMA partner universities. L.W.L. acknowledges NSF AST-1139950.

Facilities: CARMA, SST(IRAC).

REFERENCES

- Andre, P., Ward-Thompson, D., & Barsony, M. 1993, *Astrophysical Journal*, 406, 122
- Arce, H. G., & Sargent, A. I. 2004, *ApJ*, 612, 342
- Arce, H. G., Shepherd, D., Gueth, F., et al. 2007, *Protostars and Planets V*, 245
- Artymowicz, P. 1994, *ApJ*, 423, 581
- Bachiller, R., & Pérez Gutiérrez, M. 1997, *The Astrophysical Journal*, 487, L93

- Bachiller, R., & Pérez Gutiérrez, M. 1997, *ApJ*, 487, L93
- Bachiller, R., Pérez Gutiérrez, M., Kumar, M. S. N., & Tafalla, M. 2001, *Astronomy & Astrophysics*, 372, 899
- Bachiller, R., Pérez Gutiérrez, M., Kumar, M. S. N., & Tafalla, M. 2001, *A&A*, 372, 899
- Blandford, R. D., & Payne, D. G. 1982, *MNRAS*, 199, 883
- Caselli, P., Myers, P. C., & Thaddeus, P. 1995, *Astrophysical Journal Letters* v.455, 455, L77
- Cerqueira, A. H., Velázquez, P. F., Raga, A. C., Vasconcelos, M. J., & de Colle, F. 2006, *A&A*, 448, 231
- Chiang, H.-F., Looney, L. W., & Tobin, J. J. 2012, *The Astrophysical Journal*, 756, 168
- Chiang, H.-F., Looney, L. W., Tobin, J. J., & Hartmann, L. 2010, *The Astrophysical Journal*, 709, 470
- Choi, M., Kang, M., & Tatematsu, K. 2011, *ApJ*, 728, L34
- Codella, C., Bachiller, R., & Reipurth, B. 1999, *A&A*, 343, 585
- Draine, B. T. 2006, *The Astrophysical Journal*, 636, 1114
- Dunhill, A., Alexander, R., Nixon, C., & King, A. 2014, *arXiv.org*, 3842
- Fernández-López, M., Girart, J. M., Curiel, S., et al. 2013, *ApJ*, 778, 72
- Ferreira, J. 1997, *A&A*, 319, 340
- Ferreira, J., Dougados, C., & Cabrit, S. 2006, *A&A*, 453, 785
- Frank, A., Ray, T. P., Cabrit, S., et al. 2014, *arXiv.org*, 3553
- Fridlund, C. V. M., & Liseau, R. 1998, *ApJ*, 499, L75
- Gómez-Ruiz, A. I., Hirano, N., Leurini, S., & Liu, S. Y. 2013, *Astronomy & Astrophysics*, 558, 94
- Gueth, F., Guilloteau, S., & Bachiller, R. 1996, *A&A*, 307, 891
- Gueth, F., Guilloteau, S., & Bachiller, R. 1998, *Astronomy & Astrophysics*, 333, 287
- Gueth, F., Guilloteau, S., & Bachiller, R. 1998, *A&A*, 333, 287

- Gueth, F., Guilloteau, S., Dutrey, A., & Bachiller, R. 1997, *Astronomy & Astrophysics*, 323, 943
- Guilloteau, S., Dutrey, A., Pety, J., & Gueth, F. 2008, *A&A*, 478, L31
- Hildebrand, R. H. 1983, *Quarterly Journal of the Royal Astronomical Society*, 24, 267
- Itoh, Y., Kaifu, N., Hayashi, M., et al. 2000, *PASJ*, 52, 81
- Konigl, A., & Pudritz, R. E. 2000, *Protostars and Planets IV*, 759
- Kwon, W., Looney, L. W., Mundy, L. G., Chiang, H.-F., & Kemball, A. J. 2009, *The Astrophysical Journal*, 696, 841
- Launhardt, R., Pavlyuchenkov, Y., Gueth, F., et al. 2009, *A&A*, 494, 147
- Lee, C.-F., Hasegawa, T. I., Hirano, N., et al. 2010, *ApJ*, 713, 731
- Li, G., Naoz, S., Kocsis, B., & Loeb, A. 2014, *ApJ*, 785, 116
- Lim, J., & Takakuwa, S. 2006, *ApJ*, 653, 425
- Looney, L. W., Mundy, L. G., & Welch, W. J. 2000, *The Astrophysical Journal*, 529, 477
- Looney, L. W., Tobin, J. J., & Kwon, W. 2007, *The Astrophysical Journal*, 670, L131
- Masciadri, E., & Raga, A. C. 2002, *ApJ*, 568, 733
- Mathis, J. S., Rumpl, W., & Nordsieck, K. H. 1977, *Astrophysical Journal*, 217, 425
- Miettinen, O., Harju, J., Haikala, L. K., & Pomrén, C. 2006, *A&A*, 460, 721
- Montgomery, M. M. 2009, *ApJ*, 705, 603
- Müller, H. S. P., Thorwirth, S., Roth, D. A., & Winnewisser, G. 2001, *Astronomy & Astrophysics*, 370, L49
- Murphy, G. C., Lery, T., O’Sullivan, S., et al. 2008, *A&A*, 478, 453
- Nisini, B., Benedettini, M., Codella, C., et al. 2010, *Astronomy & Astrophysics*, 518, L120
- Ossenkopf, V., & Henning, T. 1994, *Astronomy and Astrophysics (ISSN 0004-6361)*, 291, 943
- Pety, J., Gueth, F., Guilloteau, S., & Dutrey, A. 2006, *A&A*, 458, 841

- Pyo, T.-S., Hayashi, M., Kobayashi, N., Tokunaga, A. T., & Terada, H. 2009, in American Astronomical Society Meeting Abstracts, Vol. 213, American Astronomical Society Meeting Abstracts #213, 605.05
- Raga, A. C., Esquivel, A., Velázquez, P. F., et al. 2009, *ApJ*, 707, L6
- Reipurth, B., Yu, K. C., Rodríguez, L. F., Heathcote, S., & Bally, J. 1999, *A&A*, 352, L83
- Rodríguez, L. F., Porras, A., Claussen, M. J., et al. 2003, *ApJ*, 586, L137
- Santangelo, G., Nisini, B., Antonucci, S., et al. 2013, *Astronomy & Astrophysics*, 557, 22
- Sault, R. J., Teuben, P. J., & Wright, M. C. H. 1995, in Astronomical Society of the Pacific Conference Series, Vol. 77, Astronomical Data Analysis Software and Systems IV, ed. R. A. Shaw, H. E. Payne, & J. J. E. Hayes, 433–+
- Shu, F., Najita, J., Ostriker, E., et al. 1994, *ApJ*, 429, 781
- Soker, N., & McIey, L. 2013, *ApJ*, 772, L22
- Stephens, I. W., Jackson, J. M., Sanhueza, P., et al. 2015, *The Astrophysical Journal*, 802, 6
- Stephens, I. W., Looney, L. W., Kwon, W., et al. 2013, *The Astrophysical Journal Letters*, 769, L15
- Takami, M., Karr, J. L., Nisini, B., & Ray, T. P. 2011, *ApJ*, 743, 193
- Teixeira, P. S., McCoey, C., Fich, M., & Lada, C. J. 2008, *MNRAS*, 384, 71
- Terquem, C., Eisloffel, J., Papaloizou, J. C. B., & Nelson, R. P. 1999a, *ApJ*, 512, L131
- Terquem, C., Papaloizou, J. C. B., & Nelson, R. P. 1999b, in Astronomical Society of the Pacific Conference Series, Vol. 160, Astrophysical Discs - an EC Summer School, ed. J. A. Sellwood & J. Goodman, 71
- Tobin, J. J., Hartmann, L., Bergin, E., et al. 2012, *The Astrophysical Journal*, 748, 16
- Tobin, J. J., Chandler, C. J., Wilner, D. J., et al. 2013, *The Astrophysical Journal*, 779, 93
- Tobin, J. J., Chandler, C. J., Wilner, D. J., et al. 2013, *ApJ*, 779, 93
- Umemoto, T., Iwata, T., Fukui, Y., et al. 1992, *Astrophysical Journal*, 392, L83
- Womack, M., Ziurys, L. M., & Wyckoff, S. 1992, *The Astrophysical Journal*, 387, 417

Zapata, L. A., Schmid-Burgk, J., Muders, D., et al. 2010, A&A, 510, A2

Zhang, Q., Ho, P. T. P., & Wright, M. C. H. 2000, AJ, 119, 1345

Table 1. CARMA observations toward L1157

Dates (UT)	Config.	Calibrators (flux/gain)	Pointings	Species
2010 Jul 22	E-array	MWC349, 1927+739	outflow (mosaic)	1 mm Cont., CO, C ¹⁷ O, CN, CH ₃ OH, H ₂ O
2010 Jul 23	E-array	MWC349, 1927+739	outflow (mosaic)	1 mm Cont., CO, C ¹⁷ O, CN, CH ₃ OH, H ₂ O
2010 Aug 04	D-array	MWC349, 1927+739	envelope	1 mm Cont., CO, C ¹⁷ O, CN, CH ₃ OH, H ₂ O
2010 Aug 05	D-array	Uranus, 1927+739	envelope	1 mm Cont., CO, C ¹⁷ O, CN, CH ₃ OH, H ₂ O
2010 Oct 17	C-array	MWC349, 1927+739	envelope	3 mm Cont., (C ¹⁸ O, ¹³ CO, N ₂ H ⁺ , CH ₃ OH, SO, SO ₂)
2010 Oct 19	C-array	MWC349, 1927+739	envelope	3 mm Cont., C ¹⁸ O, ¹³ CO, N ₂ H ⁺ , CH ₃ OH, SO, SO ₂
2010 Oct 25	C-array	MWC349, 1927+739	envelope	3 mm Cont., C ¹⁸ O, ¹³ CO, N ₂ H ⁺ , CH ₃ OH, SO, SO ₂
2011 Jul 26 ^a	E-array	MWC349, 1927+739	envelope	1 mm Cont., CO, CS

^aPolarimetric data presented in Stephens et al. (2013)

Table 2. Observational results of molecular lines toward L1157

Molecular lines	Frequencies GHz	Beams " × " (PA°)	Velocity Res. km s ⁻¹	RMS Jy bm ⁻¹ (ch ⁻¹)	Notes
1mm continuum	230.1 ¹	2.8 × 2.1 (-18)		0.0047	
CO J=2-1	230.538000	4.8 × 4.2 (72)	0.51	0.34	data mapping the outflow
CO J=2-1	230.538000	2.5 × 2.0 (-17)	0.50	0.10	data toward the envelope
C ¹⁷ O J=2-1	224.714368	2.6 × 2.2 (-15)	0.52	0.091	detected in the envelope
CS J=5-4	244.93556	6.3 × 2.6 (-28)	0.40	0.31	detected northwest of envelope
CN N,J,F=2,3/2,5/2-1,1/2,3/2	226.659543	2.6 × 2.1 (-17)	0.52	0.098	detected in the envelope
CH ₃ OH 8(-1,8)-7(0,7)	229.75876	2.5 × 2.0 (-15)	0.51	0.12	not detected
H ₂ O $v_2=1\ 5(5,0)-6(4,3)$	232.68670	2.5 × 2.1 (-16)	0.50	0.10	not detected
3mm continuum	101.4 ¹	2.1 × 1.8 (-74)		0.00044	
N ₂ H ⁺ 1-0 F ₁ =2-1 F=2-1 ^a	93.173480	2.3 × 2.0 (-75)	0.1 (0.065) ²	0.083	detected in the envelope
¹³ CO J=1-0	110.201354	1.9 × 1.7 (-74)	0.22	0.079	detected in the envelope
C ¹⁸ O J=1-0	109.782176	1.9 × 1.7 (-75)	0.1 (0.056) ²	0.084	detected in the envelope
CH ₃ OH 3(1,3)-4(0,4) A++	107.013770	2.0 × 1.7 (-76)	0.23	0.075	not detected
SO N,J=3,2-2,1	109.252212	2.0 × 1.7 (-76)	0.22	0.081	not detected
SO ₂ 3(1,3)-2(0,2)	104.029410	2.0 × 1.7 (-76)	0.23	0.065	not detected

^aNote that all the 7 hyperfine structure lines were observed in a band and this line is used as the reference frequency for the velocity.

¹The continuum frequencies are a representative value of all continuum data taken by multiple wide spectral windows.

²The values in parentheses are velocity resolutions of the original data, which have been re-binned by 0.1 km s⁻¹ for studies in this paper.

Table 3. Model fitting parameters

	<i>Jet 1</i>	<i>Jet 2</i>
s_{prec}	+1	+1
v_j (km s ⁻¹) ^a	-38±10 / 59±12	-32±12 / 85±24
α (°)	11±2	11±3
T (yr) ^b	5200±1300	7600±3500
i (°)	6±1	11±2
pa (°)	26±2	14±4
ϕ_0 (°)	340±5	138±30

^aJet velocities for the southern (negative) and northern (positive) lobes

^bLarge uncertainties are expected for the precessing period T and the jet velocity since these parameters cannot be constrained separately by the model (see Raga et al. 2009).

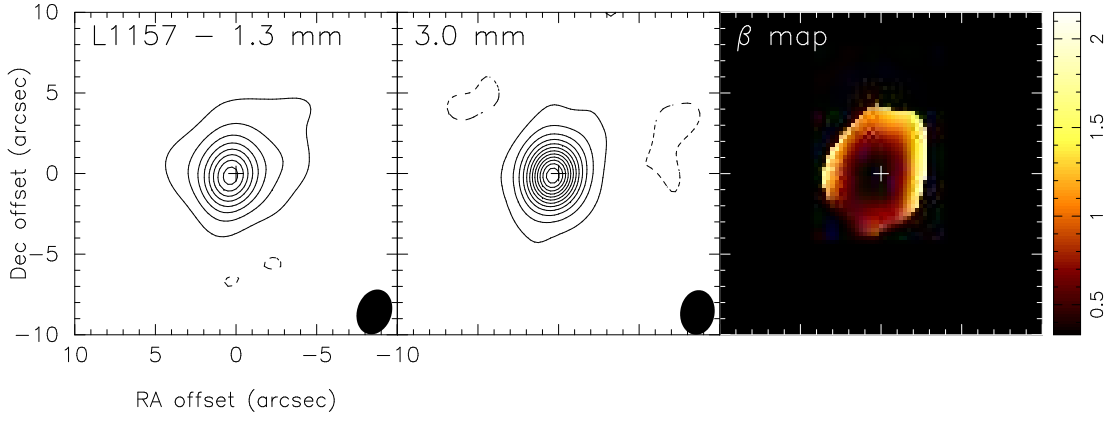


Fig. 1.— L1157 maps in continuum and the opacity spectral index β . The contour levels are $\pm 3, 9, 15, 21, 27, 33, 39, 45, 51, 57, 63$, and 69 times 4.5 and 0.5 mJy beam $^{-1}$ for $\lambda = 1.3$ and 3 mm, respectively. The β is in the range of 0.33 to 2.15 . The crosses indicate the phase center of our observations: [R.A., dec.] (J2000) = [20:39:06.20, +68:02:15.90].

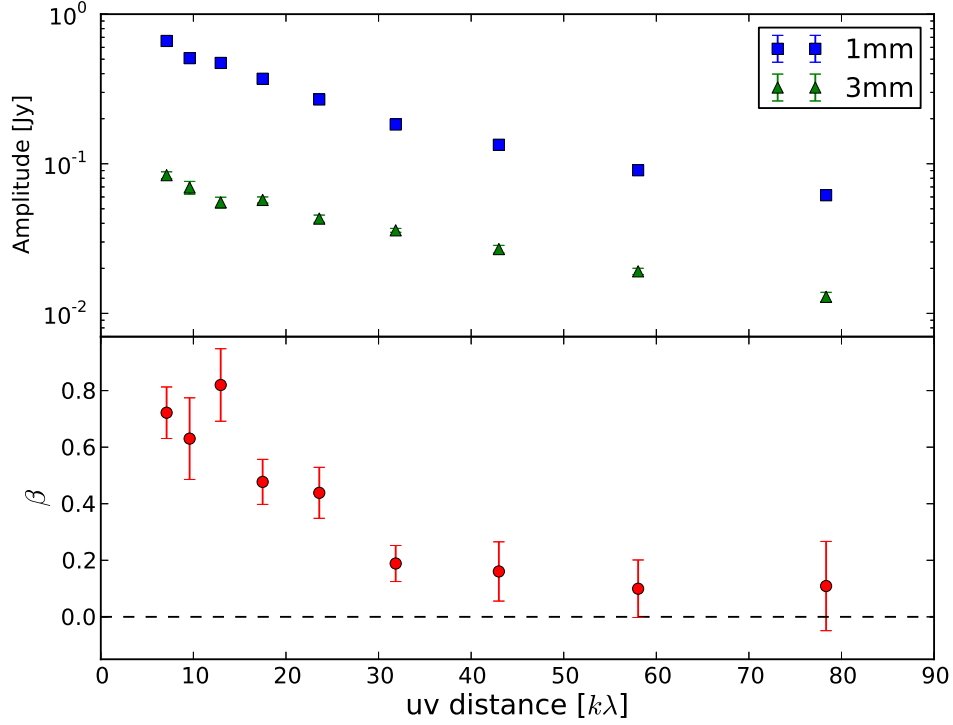


Fig. 2.— Amplitudes and β along uv distances. We obtained annulus averages of both millimeter wavelength data in logarithmic bins and calculated β in the optically thin case described in the text. The error bars indicate the β ranges varying by the statistical standard errors of annulus mean fluxes at $\lambda = 1.3$ and 3 mm. Note that the absolute flux calibration uncertainties (15% and 10% at $\lambda = 1.3$ and 3 mm, respectively) can cause a systematic error up to ± 0.35 in β (Kwon et al. 2009).

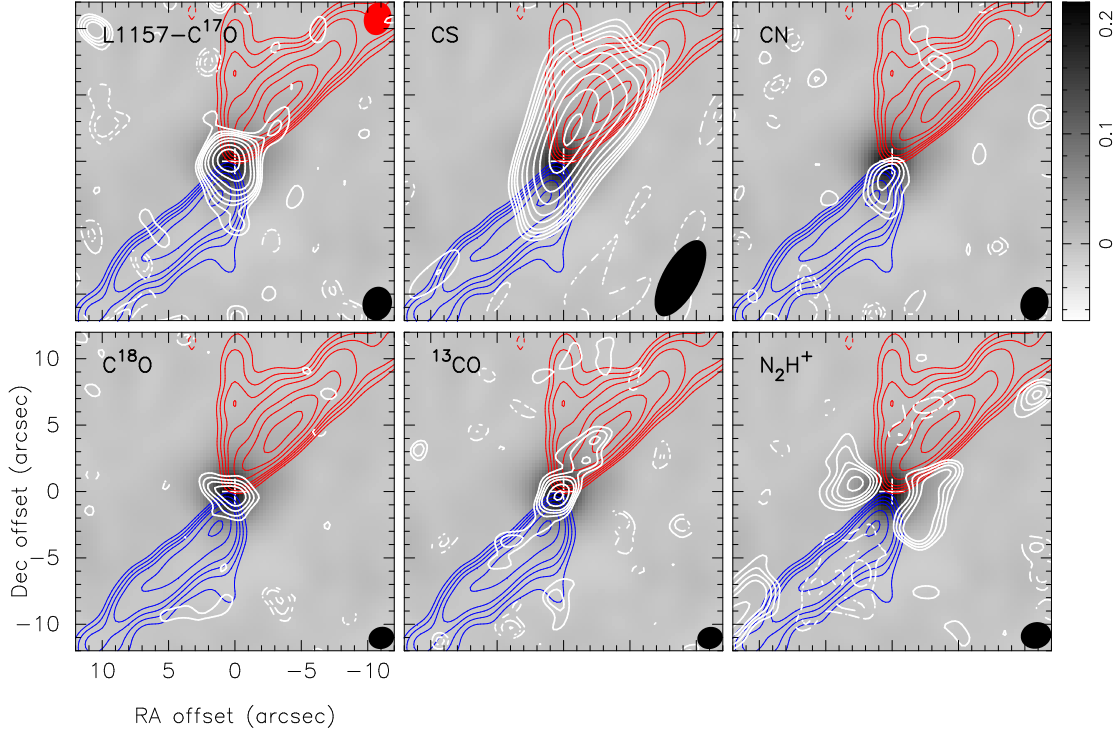


Fig. 3.— Integrated intensity maps of various molecular lines toward the L1157 envelope. The blue and red contours represent CO in velocity ranges of -22 to 2 and 4 to 30 km s^{-1} , respectively. All the contour levels are $\pm 3, 4, 5, 6, 8, 10, 13, 16, 20$, and 24 times σ : $\sigma = 2.0$ (CO), 0.080 (C^{17}O), 0.30 (CS), 0.05 (CN), 0.045 (C^{18}O), 0.055 (^{13}CO), and 0.050 (N_2H^+) $\text{Jy beam}^{-1} \text{ km s}^{-1}$. The synthesized beams are also marked at the top-right for CO data and the bottom-right for the others. The cross of each panel is the phase center. The gray scales indicate $\lambda = 1.3$ mm continuum in units of Jy beam^{-1} . The velocity ranges integrated in individual lines are: 0.83 to 4.47 km s^{-1} for C^{17}O , 1.38 to 4.17 km s^{-1} for CS, 1.25 to 3.25 km s^{-1} for CN, 1.35 to 3.95 km s^{-1} for C^{18}O , 0.35 to 5.22 km s^{-1} for ^{13}CO , and 0.59 to 3.80 km s^{-1} for N_2H^+ .

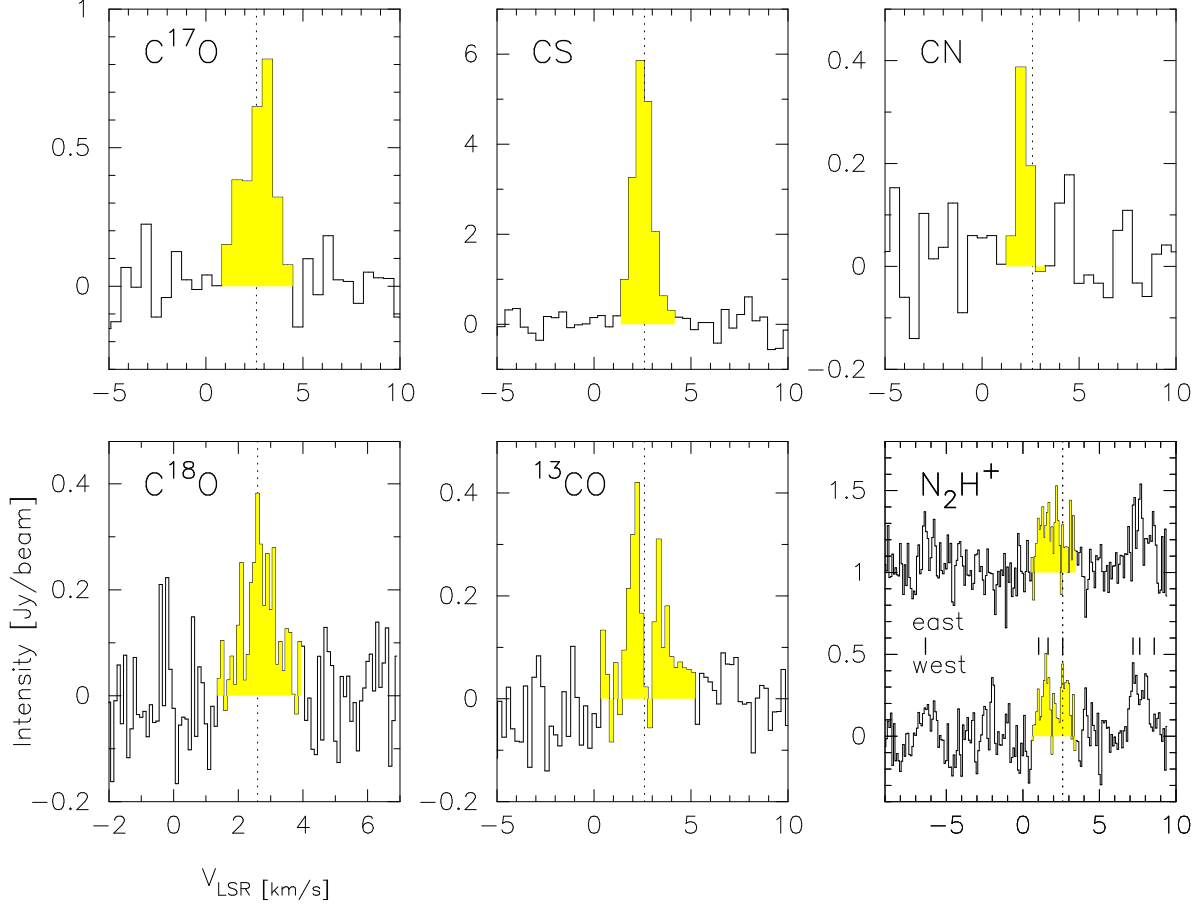


Fig. 4.— Line profiles averaged in a beam at the peak positions of the integrated intensity maps presented in Figure 3. The three CO isotope profiles have been taken at the center, as the line peak is consistent with the continuum peak. For N_2H^+ the integrated intensities of a small area at the east and west blobs are shown: a $3'' \times 3''$ box for the east and a $2'' \times 3''$ box for the west blob. The yellow shaded regions indicate the velocity regions summed up for the integrated intensity maps. For a better signal-to-noise, the C^{18}O and N_2H^+ data have been regridded in a velocity width of 0.1 km s^{-1} . The dotted vertical lines indicate the V_{LSR} of 2.6 km s^{-1} . The short solid vertical lines in the middle of the N_2H^+ panel mark the 7 hyperfine structures.

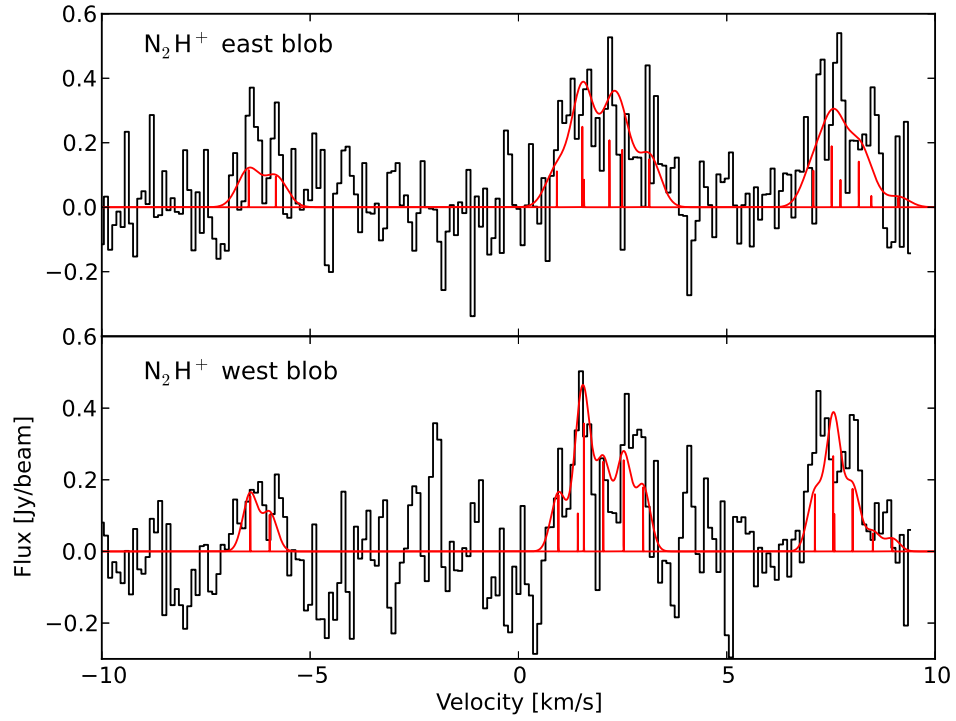


Fig. 5.— N₂H⁺ line fitting using two Gaussian profiles toward individual east and west blobs. The leftmost component is the $JF_1F = 101 \rightarrow 012$ line.

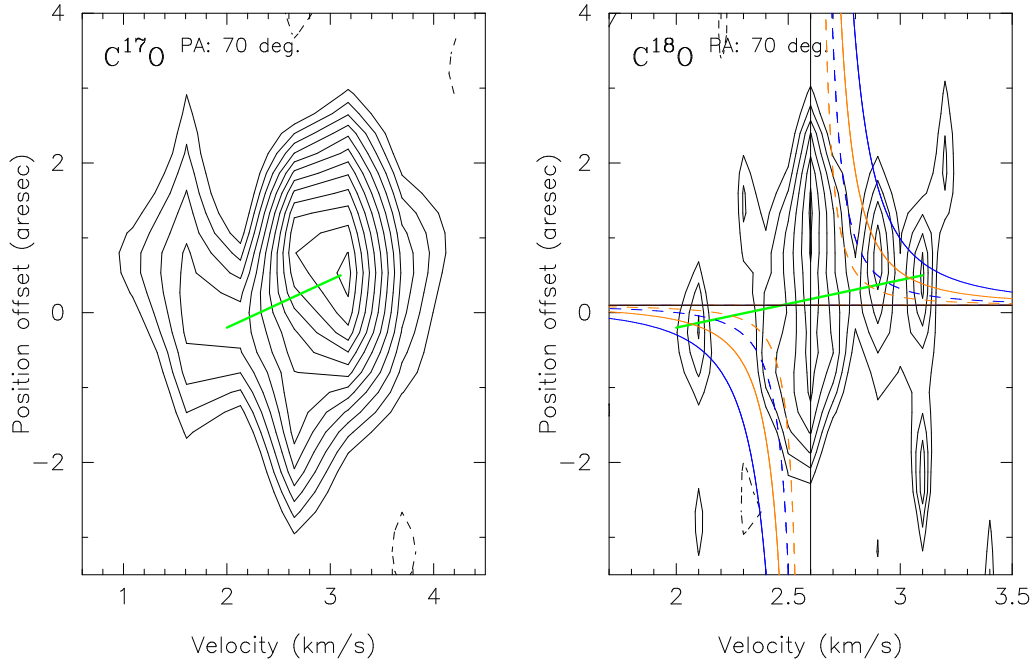


Fig. 6.— Position-velocity diagrams in C^{17}O and C^{18}O along the line perpendicular to the bipolar outflow (P.A. = 70°) through the phase center. The plus in position of the vertical axis is eastward. The lowest contours are ± 0.18 and $\pm 0.15 \text{ Jy beam}^{-1}$, and the intervals are 0.06 and $0.05 \text{ Jy beam}^{-1}$ for C^{17}O and C^{18}O , respectively. The vertical solid line of the C^{18}O diagram marks $V_{\text{LSR}} = 2.6 \text{ km s}^{-1}$ and the horizontal line indicates the location of the continuum peak, which is offset from the phase center by $0''.1$. The green lines of the two panels connect the same locations in position and velocity. The blue and orange curves indicate the Keplerian rotations around a central protostar of $0.04 M_\odot$ and $0.02 M_\odot$ at a distance of 250 pc , respectively, and the dashed lines are for the cases of a 60° inclination.

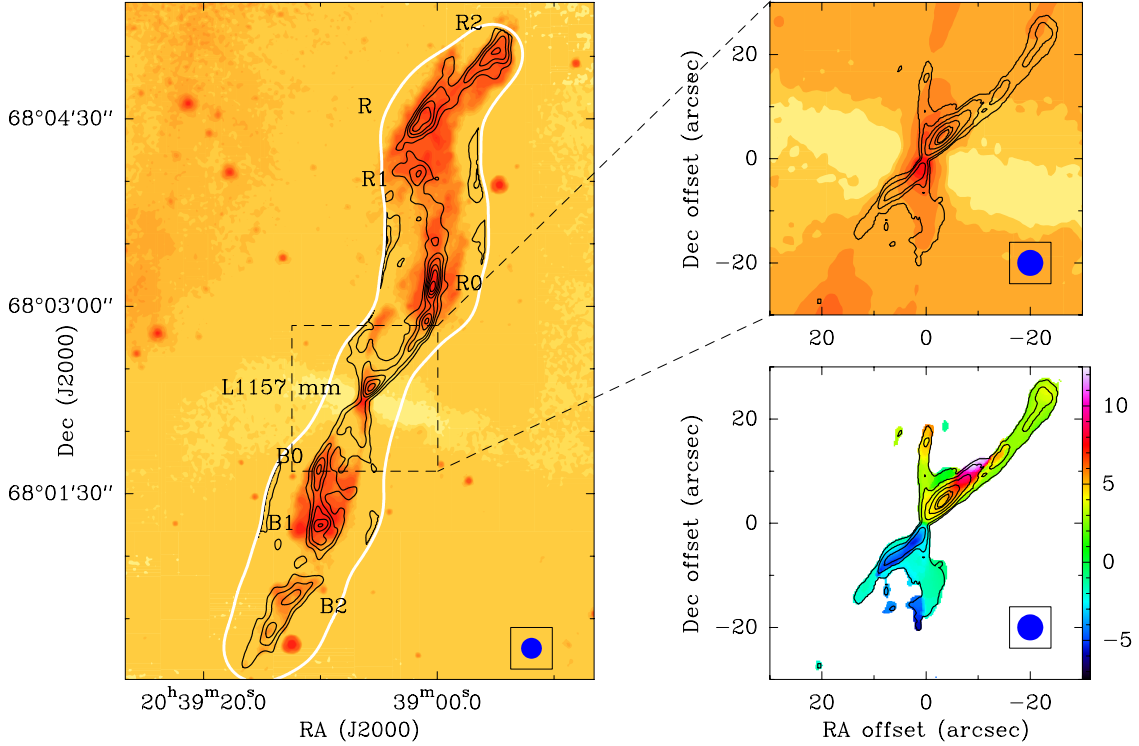


Fig. 7.— **Left:** CO CARMA E-array configuration image (black contours) on top of the 8 μm *Spitzer* image of the L1157 outflow system. The contours are 3, 8, 13, 18, 23, 28, 33 and $38 \times 3.0 \text{ Jy beam}^{-1} \text{ km s}^{-1}$ (the rms noise level is $\sim 1.3 \text{ Jy beam}^{-1} \text{ km s}^{-1}$). The positions of knots R, R0, R1, R2, B0, B1, and B2 are marked, as well as the central millimeter continuum source. The synthesized beam is plotted in the bottom right corner. The white solid line marks the area covered by the half-power primary beams of the 25 pointing mosaic. **Top right:** Zoom-in of the central part of the L1157 system. The contours show the combined CO CARMA E+D-array configuration image on top of the 8 μm *Spitzer* image. Contours are 3, 15, 35, 55, 75 and $85 \times 1.0 \text{ Jy beam}^{-1} \text{ km s}^{-1}$, the rms noise level. The synthesized beam is shown in the bottom right corner. **Bottom right:** Same as above but showing the velocity centroid (moment 1) map of the CO emission (color scale) overlaid with the integrated intensity moment 0 image (black contours).

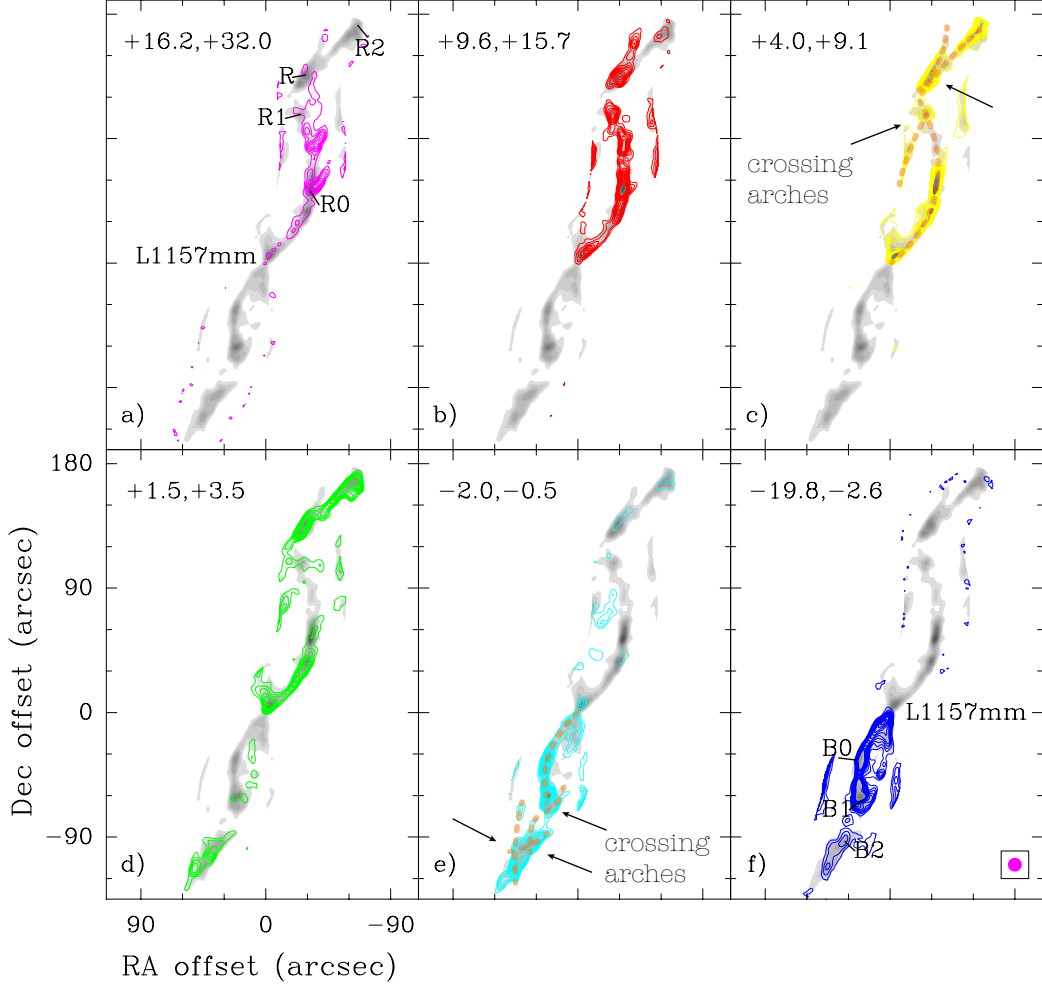


Fig. 8.— CO emission velocity map (contours) overlapped with the integrated emission (grey scale). The contours are 3, 6, 9, 12, 15, 18, 21, 24, 27 and 30 \times the rms noise level of each channel (0.7, 0.4, 0.3, 0.3, 0.4 and 0.7 Jy beam $^{-1}$ km s $^{-1}$, for a-f panels respectively). The synthesized beam is shown in the bottom right panel and the velocity interval over which each channel was integrated is indicated in each panel. In panels c) and e) the path of some arches of emission are marked with dashed orange lines.

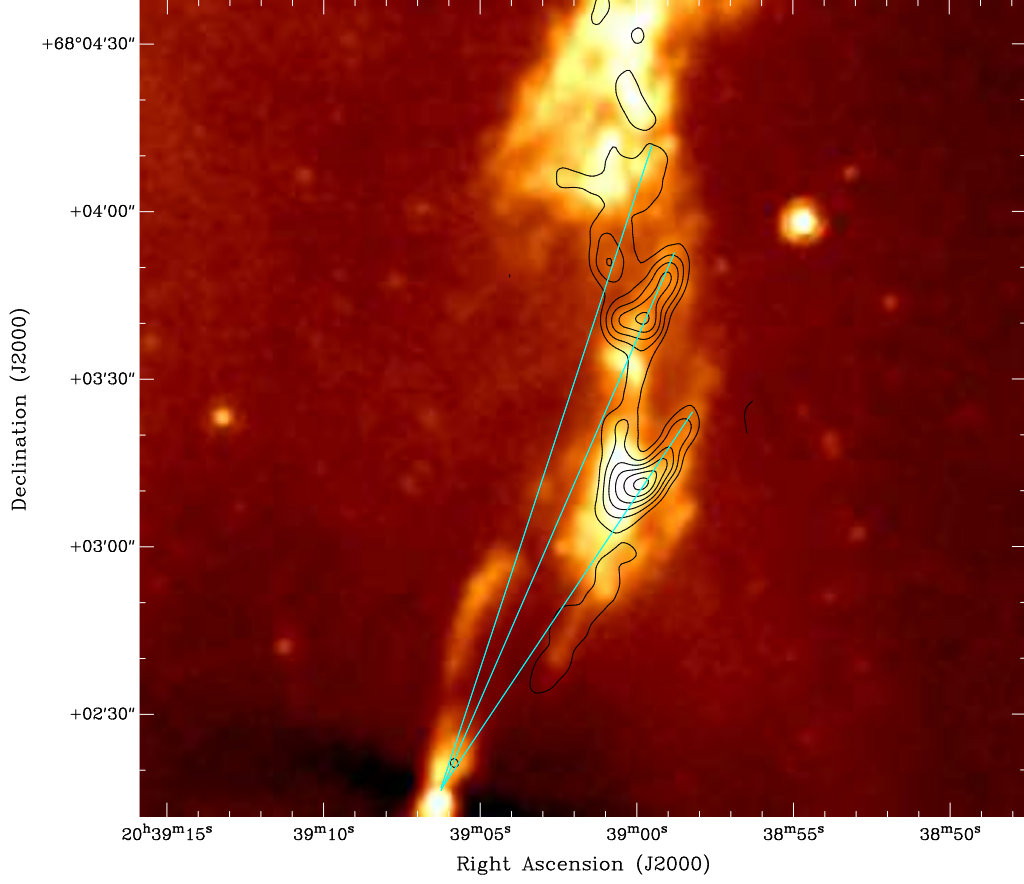


Fig. 9.— Zoom-in of the northern lobe of the L1157 outflow system. The contours show the most redshifted CO emission and the color scale is the *Spitzer* 8 μm . The contours are 15, 30, 45, 60, 75, and 90% of the peak, 15.4 Jy beam⁻¹ km s⁻¹. The blue lines indicate the ballistic trajectories of three possible molecular bullets ejected at different position angles.

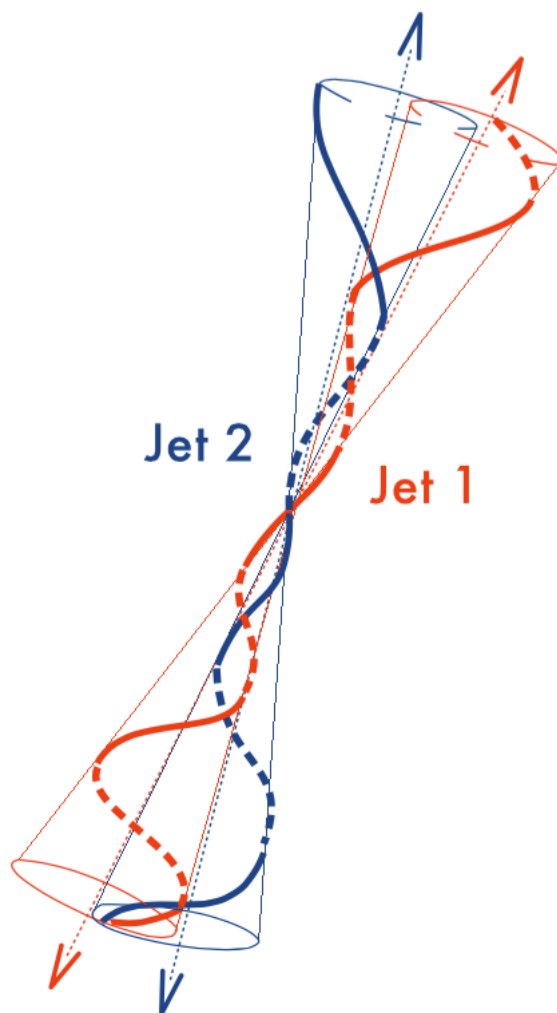


Fig. 10.— Cartoon showing the new interpretation for the L1157 outflow system as including multiple precessing molecular jets launched at different directions. Dashed lines show the path of the jets on the rear part of the cones, while solid lines show the path on the front part of the cones. The pointed arrows show the axis of symmetry of the two bipolar outflows.

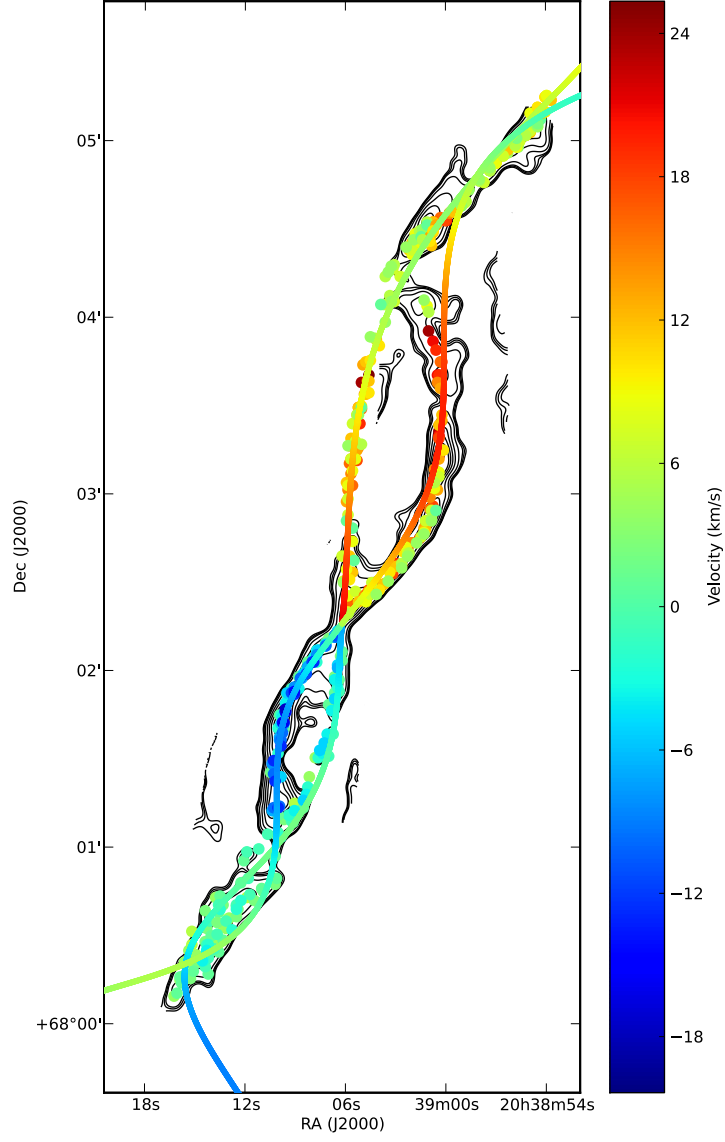


Fig. 11.— Two jet model fit (colored lines) on top of the jet points used in the fits (colored circles) and the contours representing the CARMA CO moment 0 image. The colors of the lines and points represent the velocity with respect to the cloud velocity.

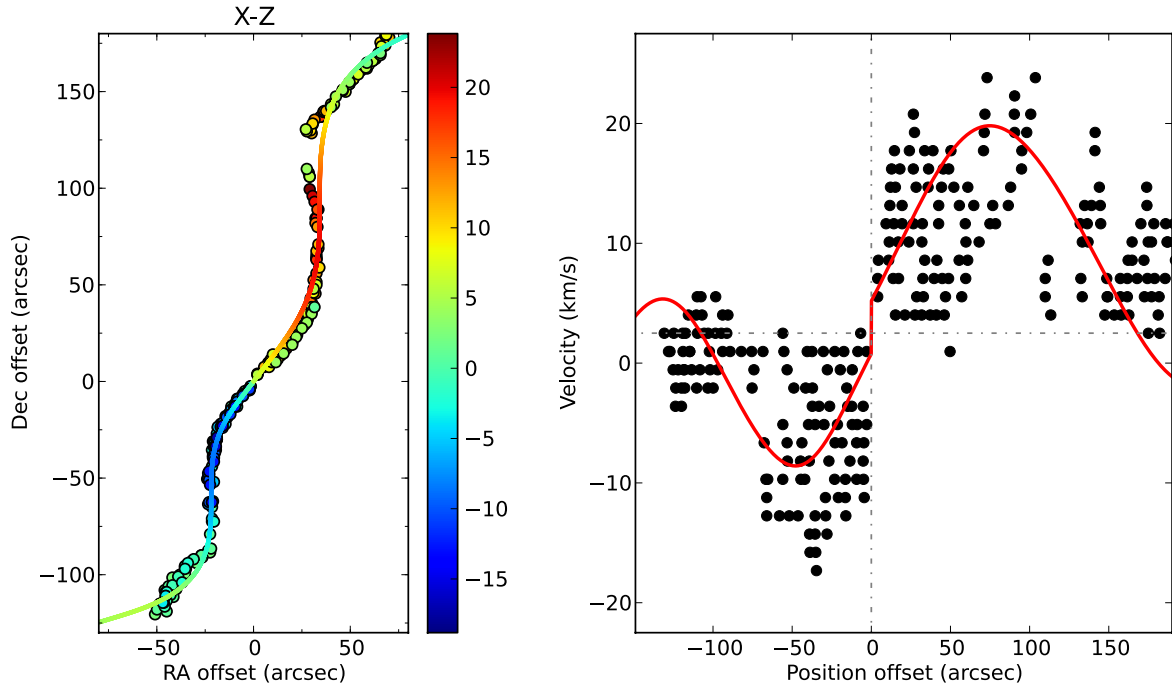


Fig. 12.— **Left:** *Jet 1* fit (colored line) on top of the jet points used in the fit (colored points). The colors represent the velocity with respect to the cloud velocity. **Right:** The plot shows the distance from the ejecting source position against the velocity of each point used to make the *Jet 1* fit (black dots). The red line shows the best fit found for this jet.

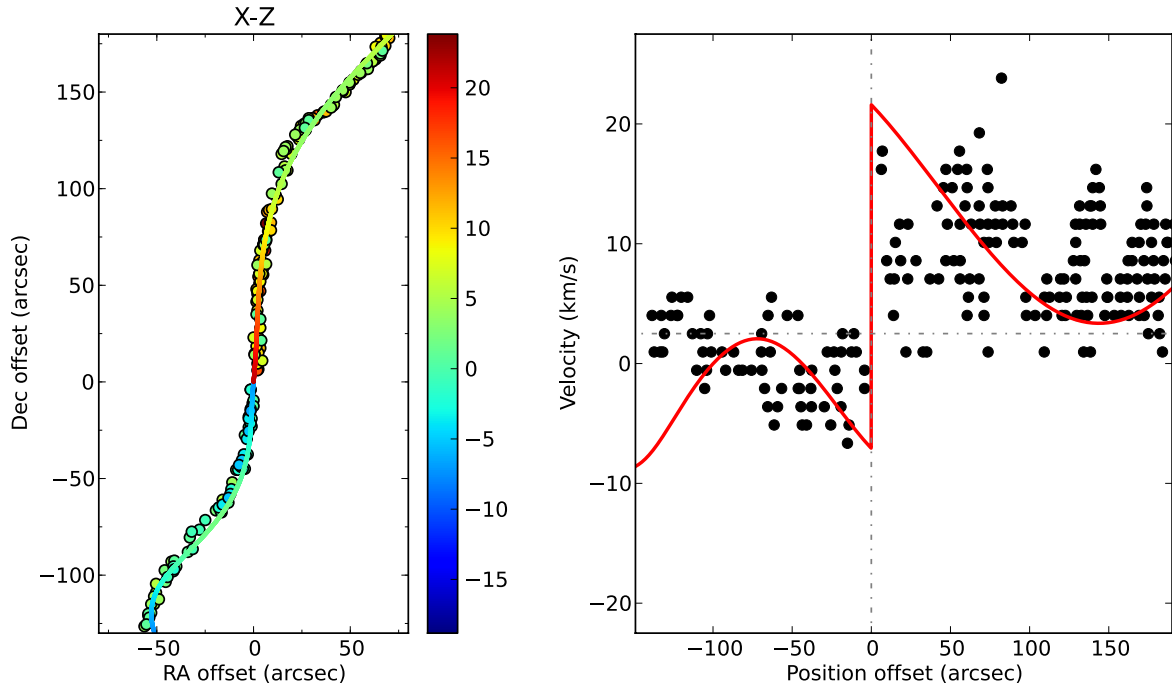


Fig. 13.— The caption is the same as Figure 12, except now is for the fit of *Jet 2*.